Acta metall. Vol. 31, No. 12, pp. 1951–1976, 1983
Printed in Great Britain. All rights reserved

0001-6160/83 $3.00 + 0.00
Copyright © 1983 Pergamon Press Ltd

OVERVIEW NO. 32

MATERIAL RATE DEPENDENCE AND LOCALIZED DEFORMATION IN CRYSTALLINE SOLIDS

D. PEIRCE,† R. J. ASARO and A. NEEDLEMAN
Division of Engineering, Brown University, Providence, RI 02912, U.S.A.

(*Received* 13 *May* 1983)

Abstract—Nonuniform deformations of rate dependent single crystals subject to tensile loading are analyzed numerically. The crystal geometry is idealized in terms of a planar double slip model. In addition to allowing the effects of material rate sensitivity to be explored, the present rate dependent formulation permits the analysis of a range of material strain hardening properties and crystal geometries that could not be analyzed within a rate independent framework. Two crystal geometries are modeled. One is a planar model of an f.c.c. crystal undergoing symmetric primary-conjugate slip. For this geometry, a direct comparison with a previous rate independent calculation shows that material rate sensitivity delays shear band development significantly. Our present rate dependent formulation also enables a more complete exploration of the effects of high (i.e. greater than Taylor) latent hardening ratios on "patchy" slip development. In particular we show that strong latent hardening and patchy slip can give rise to kinematical constraints that prevent shear bands from propagating completely across the gage section. The second geometry models a b.c.c. crystal oriented so that there is approximately a double mode of slip with the slip systems inclined by more than 45° to the tensile axis. This calculation displays the formation of a localized band of conjugate slip. The lattice rotations accompanying this mode eventually lead to a decrease in the resolved shear stress on the more active system in the band so that the bands do not accumulate large strains and catastrophic shear bands do not form. The implications of material rate sensitivity for uniqueness are also discussed with reference to implications for the prediction of mechanical properties of polycrystals.

Résumé—Nous avons analysé numériquement les déformations non uniformes de monocristaux dépendant de la vitesse, soumis à une traction. La géométrie du cristal est idéalisée en un modèle de double glissement plan. De plus, afin d'explorer les effets de la sensibilité à la vitesse du matériau, la formulation présente permet d'analyser une gamme de propriétés de durcissement et de géométries du cristal qui ne pourrait pas être analysée dans un contexte indépendant de la vitesse. Nous avons considéré deux géométries cristallines. La premiere est un modèle plan de cristal c.f.c. présentant un glissement symétrique primaire-conjugué. Pour cette géométrie, une comparaison directe avec un calcul antérieur indépendant de la vitesse montre que la sensibilité du matériau à la vitesse retarde notablement le développement des bandes de cisaillement. Notre formulation dépendant de la vitesse permet également une exploration plus complète des effets de forts rapports de durcissement latent sur le développement d'un glissement "inégal". En particulier, nous montrons qu'un fort durcissement latent et un glissement inégal peuvent produire des contraintes cinématiques qui empêchent les bandes de cisaillement de se propager entièrement à travers la section de l'éprouvette. La seconde géométrie modélise un cristal c.c. orienté de manière à ce qu'il y ait approximativement un mode double de glissement, les systèmes de glissement étant inclinés à plus de 45 degrés de l'axe de traction. Les calculs montrent la formation d'une bande localisée de glissement conjugué. Les rotations du réseau accompagnant ce mode conduisent éventuellement à une diminution de la contrainte de cisaillement réduite sur le système le plus actif dans la bande, de sorte que les bandes n'accumulent pas de grandes déformations et que de bandes de cisaillement catastrophique ne se forment pas. Nous discutons également les implications de la sensibilité à la vitesse du matériau pour la prévision des propriétés mécaniques des polycristaux.

Zusammenfassung—Die ungleichmäßige Verformung geschwindigkeitsabhängiger Einkristalle unter Zugbelastung wird numerisch analysiert. Die Kristallgeometrie wird in einem planaren Doppelgleitmodell idealisiert dargestellt. Die geschwindigkeitsabhängige Formulierung erlaubt -zusätzlich zur Untersuchung von Effekten durch die Geschwindigkeitsempfindlichkeit des Materials- die Analyse einer Reihe von Verfestigungseigenschaften und Kristallgeometrien, welche mit geschwindigkeitsunabhängigen Verfahren nicht behandelt werden können. Zwei Kristallgeometrien werden modelliert. Eine ist ein planares Modell für den kfz. Kristall, der sich in symmetrischer Gleitung im primären und im konjugierten System verformt. Bei dieser Geometrie zeigt ein Vergleich mit einer früheren geschwindigkeitsunabhängigen Rechnung, daß die Geschwindigkeitsempfindlichkeit des Materials die Entwickling von Scherbändern beträchtlich verzögert. Die vorliegende geschwindigkeitsabhängige Formulierung ermöglicht außerdem, die Effekte hoher latenter Verfestigung (d.h. größer als nach Taylor) auf das Auftreten ungleichmäßiger Gleitung zu untersuchen. Insbesondere zeigen wir, daß hohe latente Verfestigung und ungleichmäßige Gleitprozesse zu kinematischen Einschränkungen führen können, die die Ausbreitung von Scherbändern durch den gesamten Probenquerschnitt verhindern. Das zweite Modell beschreibt einen krz. Kristall, der so orientiert ist, daß annähernd Doppelgleitung auf Gleitsystemen mit mehr als 45° Neigungswinkel zur Zugachse auftritt. Die Rechnung ergibt die Bildung eines lokalisierten Bandes von konjugierter Gleitung. Die mit diesem

†Present address: Arthur D. Little, Acorn Park, Cambridge, MA 0214, U.S.A.

Gleitprozeß zusammenhängenden Gitterrotationen führen schließlich zu einem Abfall der Fließspannung in dem im Band aktiveren System. Daher können Bänder keine großen Abgleitungen akkumulieren; katastrophenartige Scherbänder treten also nicht auf. Außerdem wird die Bedeutung der Geschwindigkeitsempfindlichkeit des Materials für die Voraussage der mechanischen Eigenschaften von Polykristallen aufgezeigt.

I. INTRODUCTION

Recent rate independent finite element calculations (Peirce *et al.* [1]) of nonuniform deformation modes in ductile single crystals were based on a rate independent constitutive model for crystallographic slip. In these calculations, lattice kinematics were shown to be of particular importance in promoting nonuniform plastic flow. For example, necking was shown to cause nonuniform lattice rotations and "geometrical softening" that lead to localized shearing. The crystal lattice within shear bands was found to be characteristically misoriented with respect to the lattice in the surrounding crystal in a way that promoted geometrical softening. Geometrical softening, in this context, refers to the increase in the shear stress resolved on that slip system responsible for the concentrated straining. The results of these calculations were shown to be in very close agreement with experimental observations on necking and shear localization in single crystals of pure copper and precipitation hardened alloys of aluminum–copper and copper–cobalt. In part, this close agreement was due to the particular geometry and crystal orientation and moderate rate sensitivities of these face-centered-cubic crystals.

The analysis, however, highlighted inherent limitations of the rate independent idealization of crystalline slip. These limitations are so severe that an analysis of large strain plastic flow is precluded for a full range of material properties, in particular strain hardening properties. For this reason the constitutive theory for crystalline slip is presented here for rate dependent material response. In addition a finite element procedure based on this rate dependent constitutive law has been developed. Several calculations of tension tests have been carried out and the results are discussed in later sections. The rate dependent formulation, on the one hand, allows our previous calculations to be extended over a much broader range of material strain hardening properties and crystal geometry. This makes it possible to explore a correspondingly wider range of physical phenomena, as well as the important effects of material rate sensitivity on crystal plasticity. Just as significantly, however, the incorporation of rate dependence into the theory points the way to a reformulation of large strain crystalline plasticity in general, and for polycrystals in particular, as discussed at the end of the paper.

The limitations of the rate independent theory stem essentially from a loss of uniqueness of the "mode of slip", that is, in the choice of the actively yielding slip systems. This is a long understood difficulty in rate independent crystalline plasticity that has also been of particular concern, for example, in texture analyses. The prediction of texture in single crystals or polycrystals requires a precise specification of the slip mode to calculate lattice and grain rotations. Within the rate independent idealization of slip, uniqueness in the choice of "active" (i.e. yielding) slip systems depends fundamentally on kinematics, the crystal's strain hardening behavior and stress state. When deformations alone are prescribed, for example, uniqueness is not guaranteed when more than five linearly independent slip systems are potentially active (i.e. the resolved shear stress on them is *at* the current yield value). As Taylor originally noted [2], a *general* increment of incompressible plastic strain requires five linearly independent slip systems—with more than five available, the kinematics of straining does not, in general, uniquely specify a particular set. When stress rates are prescribed, uniqueness is not guaranteed even with fewer than five systems and, as demonstrated later, even with as few as *two* slip systems uniqueness is not generally obtainable when a full range of realistic experimental data for strain hardening behavior is used. Rate dependent formulations, on the other hand, which relate slipping rates directly, and uniquely, to the prevailing stress state (and the current material state) do allow the unique determination of the slipping rate on each slip system. This connection between material rate dependence and uniqueness of slip mode has been brought out in the recent analysis of yield vertex behavior by Pan and Rice [3].

Two types of calculations are presented below; in both cases they involve large strain tension tests of single crystals. In the first, the crystal model is identical to the one used by Peirce *et al.* [1] to model face-centered-cubic crystals deforming by a symmetric mode of primary-conjugate slip (see Fig. 2). The calculations follow the crystal through necking and the formation of shear bands, at least when the material behavior allows shear bands to form. As in the rate independent calculations, necking is found to cause nonuniform lattice rotations that produce "geometrical softening" on one or the other of the two slip systems. These rotations and the geometrical softening are the result of compatibility and represent a kind of "textural softening" within the crystal's gage section. The shear bands that form are aligned closely with one of the slip systems and, since the mode of deformation in them is nearly simple shear, the slip mode approaches single slip. The geometrical softening that develops during necking and localized shearing is caused by an increase in the resolved shear stress on that primary slip system due to lattice rotation.

Peirce *et al.* [1] demonstrated the important

influences of strain hardening and latent hardening on the localization process although, as discussed by them and as implied above, it is not possible to explore the full effects of latent hardening using a rate independent formulation. When the latent hardening rates of the slip systems are prescribed to be sufficiently larger than the self-hardening rates (i.e. sufficiently greater than for Taylor's isotropic hardening) however, the deformation rapidly becomes "patchy". This means that the crystal's gage section breaks up into contiguous regions characterized by single slip on one or the other of the potentially active slip systems or by double slip. If these differences in slip mode persist for any but very small strain increments the "patches" develop finite lattice misorientations. There is a fundamental connection between patchy slip and the question of slip mode uniqueness that clearly has important implications for both texture development and the development of deformation patterns at large strain.

For example, one of the calculations discussed in Section 3 for the f.c.c. model shown in Fig. 2 assumes a latent hardening ratio (i.e. ratio of latent hardening to self hardening) of 1.4. This ratio would, in fact, be too large to allow a corresponding rate independent calculation to be performed as in Peirce *et al.* [1]. The effect of the large ratio is to induce a pronounced pattern of patchy slip which persists for finite strains and causes misorientations of up to 10° across the patch boundaries. These large misorientations, in turn, act as "kinematical barriers" to the propagation of shear bands which initiate at the specimen's free surfaces—they prevent the bands from propagating completely through the gage. The amount of necking before failure is thus increased and failure through localized shearing may be effectively excluded.

The effects of rate sensitivity are also explored in the calculations. For the crystal model described above it is found that even moderate strain rate sensitivities, typical of f.c.c. crystals tested at 20°C or so, have very significant effects on the development of nonuniform deformation. As described below, we define the strain rate sensitivity parameter, m, as $m \equiv \partial \ln \tau^{(\alpha)} / \partial \ln \dot{\gamma}^{(\alpha)}$ where $\tau^{(\alpha)}$ and $\dot{\gamma}^{(\alpha)}$ are the resolved shear stress and the slip rate on slip system α. In one series of calculations using the f.c.c. model described above and the same material strain hardening law for various strain rate sensitivities it is found that varying m from a value of 0 to 0.005 causes a significant increase in the overall extensional strain at which shear bands appear and a much more gradual falling of load at that point. This demonstrates that even very moderate rate sensitivities which might easily be ignored in the analysis of simple tensile tests have noticeable influence on the development of localized deformation modes.

The second type of calculation presented below is again based on the crystal model of Fig. 2 but with $\phi = 60°$ initially. There are orientations for b.c.c. crystals for which the slip mode is approximately a double mode of slip where the slip systems are inclined by more than 45° to the tensile axes. An example is found in the experiments conducted by Reid *et al.* [4] on pure niobium. As discussed below, whether ϕ is greater than, or less than, 45° is important in this model for determining uniqueness of the slip mode and the mathematical character of the equations governing plastic flow. The material properties are chosen to approximate those of niobium when tested at around 20°C. Catastrophic shear bands do not form; instead the crystals undergo substantial necking. In fact, although this calculation does not display shear bands it does show the formation of a localized band of conjugate slip. In particular, well defined bands of concentrated slip develop on slip systems such that the *lattice* rotation accompanying this strain eventually leads to a *decrease* in the resolved shear stress on the more active system. Furthermore, the orientation of these bands is much more closely aligned with the less active slip system so that these bands resemble what have been called "bands of secondary slip" in the literature. An example of such a band is shown in Fig. 1. Such bands do not accumulate strains large enough to cause fracture but certainly affect the development of texture and overall strain hardening in the gage section.

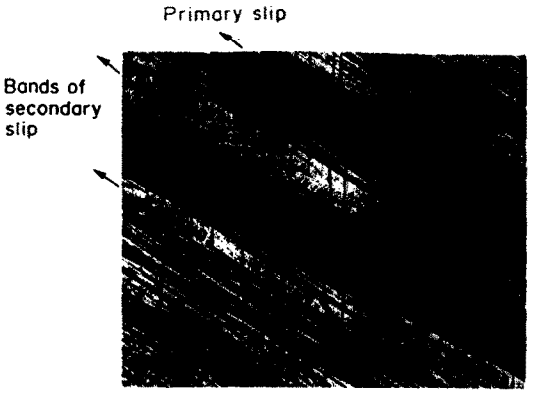

Fig. 1. Optical micrograph of "bands of secondary slip" formed in an aluminum single crystal taken from Sawkill and Honeycombe [5]. The bands are closely aligned with what is designated as the primary slip system but are characterized by slip on a "secondary" slip system.

The plan of the paper is as follows: in Section 2.1 the constitutive laws for rate dependent crystals are developed; in Section 2.2 the crystal hardening laws are discussed; in Section 2.3 the specific model used in the calculations is presented and some analysis is done for the rate independent version to understand questions of uniqueness and stability; in Section 3 the numerical procedures and results are presented followed by discussion in Section 4.

2. THE CRYSTAL MODEL

2.1. *Constitutive laws for rate dependent crystals*

The kinematical basis underlying the constitutive description used here for rate dependent single crystals is identical to that employed in a previous rate independent analysis (Peirce *et al.* [1]). This

formulation stems from the early work of Taylor and Elam [6, 7] and Taylor [2] who established a quantitative description of plastic deformation in single crystals based on crystallographic shearing. Rice [8] and Hill and Rice [9] later developed a general finite deformation elastic-plastic framework for analyzing the deformations of rate independent single crystals. In this section, the constitutive laws are developed for rate dependent crystals.

The deformation gradient $\mathbf{F}$ is written as

$$\mathbf{F} = \mathbf{F}^* \cdot \mathbf{F}^p. \tag{2.1}$$

The deformation embodied in $\mathbf{F}^p$ consists solely of crystallographic slipping along specific slip systems $(\mathbf{s}, \mathbf{m})$, where $\mathbf{s}$ is the unit slip direction and $\mathbf{m}$ is the unit slip plane normal. Elastic stretching and rotation are included in $\mathbf{F}^*$, which also accounts for any rigid body rotations.

Since $\mathbf{s}$ and $\mathbf{m}$ are regarded as lattice vectors, they are stretched and rotated as follows

$$\mathbf{s}^* = \mathbf{F}^* \cdot \mathbf{s}, \quad \mathbf{m}^* = \mathbf{m} \cdot \mathbf{F}^{*-1}. \tag{2.2}$$

The vectors $\mathbf{s}^*$ and $\mathbf{m}^*$, orthogonal since $\mathbf{s}$ and $\mathbf{m}$ are, characterize a particular slip system in the deformed configuration. The plastic part of the Eulerian velocity gradient, $\dot{\mathbf{F}} \cdot \mathbf{F}^{-1}$, is thus given by

$$\dot{\mathbf{F}} \cdot \mathbf{F}^{-1} - \dot{\mathbf{F}}^* \cdot \mathbf{F}^{*-1} = \mathbf{F}^* \cdot \dot{\mathbf{F}}^p \cdot \mathbf{F}^{p-1} \cdot \mathbf{F}^{*-1}$$

$$= \sum_\alpha \dot{\gamma}^{(\alpha)} \mathbf{s}^{*(\alpha)} \mathbf{m}^{*(\alpha)} \tag{2.3}$$

where the rate of shearing is $\dot{\gamma}^{(\alpha)}$ on slip system α. Note that $\dot{\mathbf{F}}^* \cdot \mathbf{F}^{*-1}$ is the elastic portion. The rightmost equality of (2.3) is equivalent to the expression for the rate $\dot{\mathbf{F}}^p$ given by Rice [8]

$$\dot{\mathbf{F}}^p = \sum_\alpha \dot{\gamma}^{(\alpha)} \mathbf{s}^{(\alpha)} \mathbf{m}^{(\alpha)} \cdot \mathbf{F}^p. \tag{2.4}$$

One may define symmetric (stretching) and antisymmetric (spin) parts of (2.3) as

$$\mathbf{D}^p = \sum_\alpha \mathbf{P}^{(\alpha)} \dot{\gamma}^{(\alpha)} \tag{2.5}$$

and

$$\boldsymbol{\Omega}^p = \sum_\alpha \mathbf{W}^{(\alpha)} \dot{\gamma}^{(\alpha)} \tag{2.6}$$

where the tensors $\mathbf{P}^{(\alpha)}$ and $\mathbf{W}^{(\alpha)}$ are given by

$$\mathbf{P}^{(\alpha)} = \tfrac{1}{2}(\mathbf{s}^{*(\alpha)} \mathbf{m}^{*(\alpha)} + \mathbf{m}^{*(\alpha)} \mathbf{s}^{*(\alpha)}) \tag{2.7}$$

and

$$\mathbf{W}^{(\alpha)} = \tfrac{1}{2}(\mathbf{s}^{*(\alpha)} \mathbf{m}^{*(\alpha)} - \mathbf{m}^{*(\alpha)} \mathbf{s}^{*(\alpha)}). \tag{2.8}$$

Sums over slip systems are shown explicitly in this paper, and thus no sum is implied in (2.7) or (2.8). The elastic rates of stretching and spin, $\mathbf{D}^*$ and $\boldsymbol{\Omega}^*$, are the symmetric and antisymmetric parts of $\dot{\mathbf{F}}^* \cdot \mathbf{F}^{*-1}$, so that the total rates of stretching and spin are

$$\mathbf{D} = \mathbf{D}^* + \mathbf{D}^p \tag{2.9}$$

$$\boldsymbol{\Omega} = \boldsymbol{\Omega}^* + \boldsymbol{\Omega}^p. \tag{2.10}$$

The crystal elasticity is presumed to be unaffected by slip, whence the usual tensor of elastic moduli $\mathbf{L}$ relates the lattice Jaumann rate of Kirchhoff stress to the elastic rate of stretching

$$\overset{\nabla}{\boldsymbol{\tau}}{}^* = \mathbf{L} : \mathbf{D}^*. \tag{2.11}$$

By (2.6), $\overset{\nabla}{\boldsymbol{\tau}}{}^*$ is related to the material Jaumann rate of Kirchhoff stress via

$$\overset{\nabla}{\boldsymbol{\tau}}{}^* = \overset{\nabla}{\boldsymbol{\tau}} + \sum_\alpha \boldsymbol{\beta}^{(\alpha)} \dot{\gamma}^{(\alpha)} \tag{2.12}$$

where

$$\boldsymbol{\beta}^{(\alpha)} = \mathbf{W}^{(\alpha)} \cdot \boldsymbol{\tau} - \boldsymbol{\tau} \cdot \mathbf{W}^{(\alpha)}. \tag{2.13}$$

Equations (2.9), (2.11) and (2.12) lead to

$$\overset{\nabla}{\boldsymbol{\tau}} = \mathbf{L} : \mathbf{D} - \sum_\alpha \mathbf{R}^{(\alpha)} \dot{\gamma}^{(\alpha)} \tag{2.14}$$

where the tensors $\mathbf{R}^{(\alpha)}$ are simply given by

$$\mathbf{R}^{(\alpha)} = \mathbf{L} : \mathbf{P}^{(\alpha)} + \boldsymbol{\beta}^{(\alpha)}. \tag{2.15}$$

In the present rate dependent formulation each $\dot{\gamma}^{(\alpha)}$ is taken to depend on the current resolved shear stress on slip system α and on other parameters which are determined by the current internal structure. It is in this respect that the rate dependent formulation fundamentally differs from the corresponding rate independent formulation where the shear rates $\dot{\gamma}^{(\alpha)}$ depend on the resolved shear stress *rates*.

The resolved shear stress on slip system α is

$$\tau^{(\alpha)} = \mathbf{s}^{*(\alpha)} \cdot \boldsymbol{\tau} \cdot \mathbf{m}^{*(\alpha)} = \mathbf{P}^{(\alpha)} : \boldsymbol{\tau}. \tag{2.16}$$

The expression used here for the shear rates $\dot{\gamma}^{(\alpha)}$ is of the power law form used by Hutchinson [10] and Pan and Rice [3]

$$\dot{\gamma}^{(\alpha)} = \dot{a}^{(\alpha)} \left[\frac{\tau^{(\alpha)}}{g^{(\alpha)}}\right] \left[\left|\frac{\tau^{(\alpha)}}{g^{(\alpha)}}\right|\right]^{(1/m)-1}. \tag{2.17}$$

The functions $g^{(\alpha)}$ characterize the current strain hardened state of the crystal. In what follows we simply take each $g^{(\alpha)}$ to depend on the sum, γ, of the slip magnitudes; i.e.

$$g^{(\alpha)} = g^{(\alpha)}(\gamma) \tag{2.18}$$

where

$$\gamma = \sum_\alpha |\gamma^{(\alpha)}| \tag{2.19}$$

and in effect we do not attempt to model Bauschinger effects. For the calculations that we will report on here this is not an important restriction.

If the rate of shearing on system α is $\dot{a}^{(\alpha)}$ throughout the deformation history then the resolved shear stress on that system $\tau^{(\alpha)}$ is equal to $g^{(\alpha)}(\gamma)$. Thus $\tau^{(\alpha)} = g^{(\alpha)}(\gamma)$ may be viewed as a reference τ–γ relation for each slip system, while $\dot{a}^{(\alpha)}$ represents the corresponding reference rate of shearing. The exponent $1/m$ characterizes the material rate sensitivity; the rate independent limit corresponds to $m = 0$.

The material strain hardening is specified by the evolution of the functions $g^{(\alpha)}(\gamma)$. The value of each $g^{(\alpha)}$

for $\gamma = 0$ must be specified; for each slip system we take this initial value to be a constant τ_0. Then, the rate of increase of the functions $g^{(\alpha)}$ is specified by

$$\dot{g}^{(\alpha)} = \sum_{\beta} h_{\alpha\beta}|\dot{\gamma}^{(\beta)}| \tag{2.20}$$

where the $h_{\alpha\beta}$ are functions of γ (2.19).

In this formulation, there is no explicit yielding; if the resolved shear stress on a system is non-zero, then plastic shearing occurs. However, for values of the rate sensitivity exponent m employed here ($m \leq 0.02$) the plastic shearing rate on systems with a resolved shear stress less than τ_0 is exceedingly small. Since within the present formulation all systems are potentially active, it is neither necessary nor convenient to consider $(\mathbf{s}^{(\alpha)}, \mathbf{m}^{(\alpha)})$ and $(-\mathbf{s}^{(\alpha)}, \mathbf{m}^{(\alpha)})$ as separate slip systems on each of which only positive slip is allowed. Thus, we permit $\dot{\gamma}^{(\alpha)}$ to be negative if the corresponding $\tau^{(\alpha)}$ is negative. This sign convention is embodied in (2.17).

The form of the hardening moduli $h_{\alpha\beta}$ matrix used here is that used earlier by Hutchinson [11], Asaro [12] and Peirce *et al.* [1]

$$h_{\alpha\beta} = qh + (1-q)h\delta_{\alpha\beta}. \tag{2.21}$$

Here, the parameter q sets the level of latent hardening as compared to the "self hardening" of the slip systems. As discussed by Peirce *et al.* [1] with $1 \leq q \leq 1.4$, latent hardening ratios observed experimentally, at finite strains, can be described using (2.21) in the rate independent theory. This is discussed in more detail in Section 2.2. It should be mentioned that a slightly different form for $h_{\alpha\beta}$ was used in the rate independent formulation of Peirce *et al.* [1], viz.

$$h_{\alpha\beta} = qh + (1-q)h\delta_{\alpha\beta} + \tfrac{1}{2}(\boldsymbol{\beta}^{(\alpha)} : \mathbf{P}^{(\beta)} - \boldsymbol{\beta}^{(\beta)} : \mathbf{P}^{(\alpha)}). \tag{2.22}$$

The purpose of the last terms in (2.22) is to preserve the symmetry structure of the rate independent constitutive law. In the rate independent case, this permits the governing equations to be cast in variational form. The variational structure is useful analytically, in that it allows questions of bifurcation and uniqueness to be addressed within the framework laid out by Hill [13], and numerically, in that it leads to a symmetric finite element stiffness matrix. For rate dependent crystals, the variational structure is not directly applicable. In the present rate dependent analysis the extra terms of (2.22) are *not* included in the formulation. It should also be noted that, in any case, these terms vanish identically in symmetric double slip.

In the present calculations $h(\gamma)$ is specified by

$$h(\gamma) = h_0 \operatorname{sech}^2\left(\frac{h_0\gamma}{\tau_s - \tau_0}\right). \tag{2.23}$$

This functional form was also employed in our previous rate independent analysis, Peirce *et al.* [1]. The constant h_0 represents an initial hardening rate, and τ_s denotes a saturation strength. As mentioned previously, τ_0 is $g^{(\alpha)}(0)$ for each slip system α.

Equation (2.14), when taken in conjunction with (2.17) and the above hardening description, defines the constitutive law used in the present study.

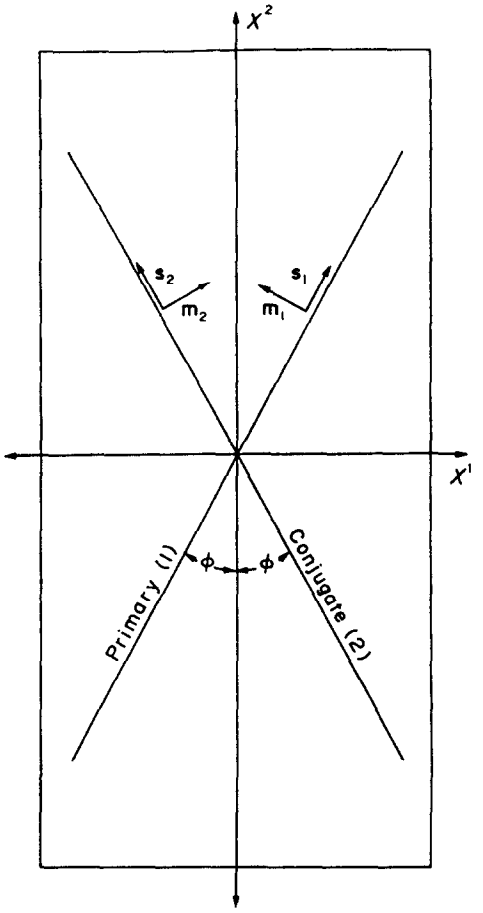

Fig. 2. A plane model for a crystal undergoing double slip. When $\phi = 30°$ this serves as a model for an f.c.c. crystal undergoing symmetric primary-conjugate slip.

2.2. *The hardening matrix and latent hardening*

As recent analyses have illustrated, there is an intimate connection between latent hardening and the stability and uniformity of plastic flow in single crystals (Asaro [12]; Peirce *et al.* [1]). In this section we confine attention to homogeneous tensile straining and begin by providing a description of overshoot using the hardening description (2.17)–(2.21) in conjunction with (2.23). This is done in order to obtain a realistic description of the range of the parameter q in (2.21). The analysis is carried out within the context of Asaro's [12] planar crystal model shown in Fig. 2.

Because of the important consequences of the detailed specification of the hardening matrix $\mathbf{h}$ for stability, we compare the overshoot predictions based on (2.21) with analogous results obtained using the hardening matrix (2.22) which was employed in our previous rate independent analysis (Peirce *et al.* [1]). Specifically, we calculate the lattice rotation that occurs in a crystal initially oriented for single slip. This models one method used to measure latent hardening whereby deviations of measured lattice rotations from predicted

single slip values are used to infer the onset of plastic deformation on latent systems.

We consider a crystal initially deforming in single slip on system p in Fig. 3. The material is modeled as rigid plastic since lattice elasticity has a negligible effect on overshoot. The neglect of lattice deformation implies that $\mathbf{F}^*$ in (2.1) is a pure rotation matrix. The requirement that a fiber initially aligned with the tensile axis remain aligned with the tensile axis gives an expression for the angle β by which the lattice has rotated, viz.

$$\tan \beta = F^p_{12}/F^p_{22}. \tag{2.24}$$

At any stage of the deformation history, the resolved shear stresses on the primary $^{(p)}$ and conjugate $^{(c)}$ systems in Fig. 3 are given by

$$\tau^{(p)} = \frac{\sigma}{2} \sin(2\phi - 2\beta) \tag{2.25}$$

$$\tau^{(c)} = \frac{\sigma}{2} \sin(2\psi + 2\beta). \tag{2.26}$$

Using (2.24) to (2.26) and the constitutive description

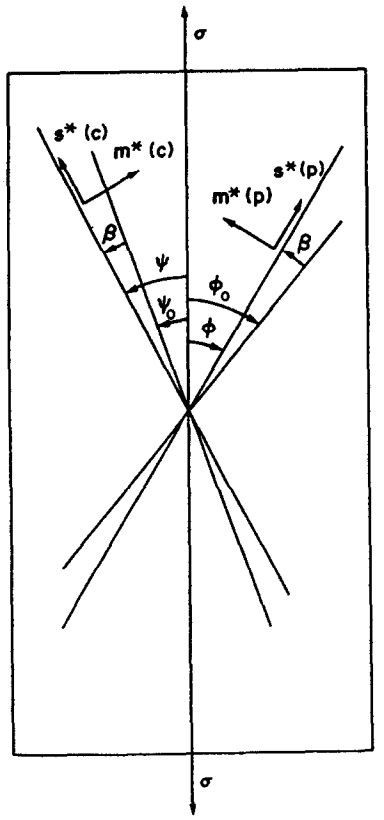

Fig. 3. The plane model shown in Fig. 2 used to calculate the amount of overshooting of the symmetric primary-conjugate orientation expected from different levels of latent hardening. Initially the crystal deforms by single slip on the primary slip system, *p*. As the lattice rotates through the angle β the resolved shear stress and slip activity increase on the conjugate slip system, *c*. If $\phi + \psi = 60°$ and $\phi = 40°$ initially, a rotation of $\beta = 10°$ brings the crystal into the symmetric orientation; $\beta > 10°$ implies "overshoot".

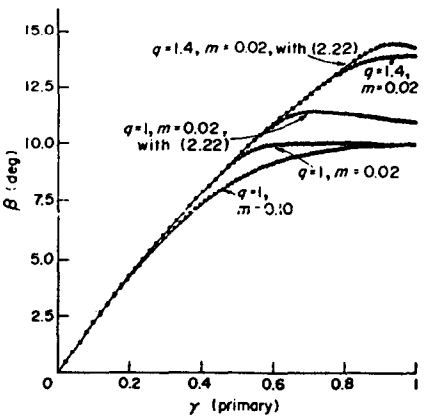

Fig. 4. Results for overshoot for different values of q and m.

presented in Section 2.1, the angle β can be computed as a function of the imposed tensile deformation. The calculation procedure is described by Asaro [14]. Figure 4 depicts the lattice rotation angle β as a function of slip on the primary system, $\gamma^{(p)}$, for several latent hardening descriptions. In each case the hardening law (2.23) is used with $h = 8.9\tau_0$ and $\tau_s = 1.8\tau_0$. The initial orientation was taken to be $\phi = 40°$ and $\psi = 20°$ so that $\phi + \psi = 60°$ corresponding to the angle between the primary and conjugate slip directions in f.c.c. crystals. When the hardening matrix (2.21) is employed with $q = 1$ (Taylor hardening), the lattice monotonically rotates to the symmetry position. Conjugate slip initiates before the symmetry boundary of $\beta = 10°$ is reached; the greater the rate sensitivity the greater the amount of slip that occurs prior to the symmetry boundary. When the hardening matrix (2.22) is employed some overshoot occurs, due to the extra terms involving stress, even if $q = 1$. However slip on the conjugate system induces reverse rotation so that after a maximum rotation of 1.5° there is a tendency to rotate back to the symmetry boundary. The peak overshoot in Fig. 4 agrees well with the amount of overshoot obtained by Peirce *et al.* [1] using a rate independent analysis. For value of $q > 1$ the behavior is qualitatively similar in that the hardening matrix (2.21) leads to an asymptotic approach to a stable orientation (the orientation itself, of course, depends on the value of q) while the hardening matrix (2.22) gives a maximum rotation followed by a rotation back to the symmetry boundary. As illustrated in Fig. 4 the detailed specification of the hardening matrix has a noticeable effect on the predicted history of lattice rotations. Asaro [14] employed a different description of the hardening matrix from either alternative considered here and his results, although giving overshoot angles in general agreement with those in Fig. 4, differ in actual detail from the present results.

Observations on overshoot have been reviewed by Peirce *et al.* [1] and Asaro [14]. They conclude, as suggested by Kocks [15], that the range 1–1.4 for the ratio of latent hardening rates to self hardening rates provides an estimate of latent hardening in f.c.c. single

crystals broadly consistent with observations. For f.c.c. pure metals and alloys overshoot angles of from 0° to 4° encompasses a good deal of the experimental data and this is the range of overshoot depicted in Fig. 4. It is also worth noting that in many reported cases (e.g. Chang and Asaro [16]), conjugate slip has been observed to occur before the loading axis has reached the symmetry line. The onset of some conjugate slip prior to the symmetry boundary is characteristic for rate dependent constitutive relations of the sort employed here. It is only in the rate independent limit that the onset of conjugate slip is abrupt.

These analyses of latent hardening provide a basis for specifying parameters in the constitutive description which have important consequences for the stability of plastic flow. Within the current rate dependent context the investigation of the stability of plastic flow requires the solution of an initial-boundary value problem. By way of contrast in the rate independent case the stability of plastic flow can be investigated in many circumstances of interest by means of a bifurcation analysis. Our numerical results will show that, although a bifurcation analysis is not directly applicable here, the overall picture of instability and localization given by such an analysis is indeed relevant in the present context. Therefore in order to provide a perspective on the numerical results we will briefly review some results of a rate independent bifurcation analysis.

2.3. *Slip mode uniqueness and bifurcation*

2.3.1. The plane crystal model. As mentioned earlier, the calculations presented in this paper are based on the planar model of a crystal undergoing a double mode of primary–conjugate shear shown in Fig. 2. In this section, we consider a crystal undergoing homogeneous tension under the uniform stress state $\sigma_{22} = \sigma$, $\sigma_{11} = \sigma_{12} = 0$ with *both* slip systems active. If the crystal's elasticity is taken to be incompressible, the model is that of a plane, orthotropic, incompressible solid and so falls into the wide class of such models studied by Biot [17] and more recently by Hill and Hutchinson [18]. For a rate independent material the incremental response is governed by just two instantaneous moduli: μ governing shear parallel to the x_1, x_2 coordinate axes and μ^* governing shear at 45° to them. The constitutive laws take the form

$$\overset{\nabla}{\sigma}_{22} - \overset{\nabla}{\sigma}_{11} = 2\mu^*(D_{22} - D_{11}) \tag{2.27$_1$}$$

$$\overset{\nabla}{\sigma}_{12} = 2\mu D_{12} \tag{2.27$_2$}$$

along with the incompressibility condition

$$D_{11} + D_{22} = 0. \tag{2.27$_3$}$$

For the model shown in Fig. 2

$$\mu^* = \frac{Gh^*(1+q)}{h^*(1+q) + 2G\sin^2 2\phi^*} \tag{2.28}$$

and

$$\mu = \frac{G(h^*(1-q) + \sigma\cos 2\phi^*) - \sigma^2/2}{h^*(1-q) + 2G\cos^2 2\phi^* - \sigma\cos 2\phi^*} \tag{2.29}$$

with

$$h^*\left(\frac{ds^*}{ds}\right)^4 = h \tag{2.30$_1$}$$

and

$$\lambda^{*2}\tan\phi^* = \tan\phi. \tag{2.30$_2$}$$

ds^*/ds is the *elastic* stretch ratio in either slip direction, and λ is the elastic stretch ratio in the tensile direction. For practical purposes, elastic stretching is negligible and it is convenient to represent μ and μ^* as

$$\mu^* = \frac{h(1+q)}{2\sin^2 2\phi} \tag{2.31$_1$}$$

and

$$\mu = \frac{h(1-q) + \sigma\cos 2\phi}{2\cos^2 2\phi}. \tag{2.31$_2$}$$

The bifurcation results given by Hill and Hutchinson [18] can be used to predict the onset of shear bands. This is done by studying the character of the equations governing elastic–plastic flow and determining when they become nonelliptic and thereby admit real characteristics. Since this will be done using the constitutive laws given above, it is important to recall that they are based on an assumed double mode of slip. It is therefore important to examine the conditions which guarantee that this slip mode is unique. As it happens, the sufficiency conditions will fail when applied using the full range of experimental data for material strain hardening and latent hardening even for this simple crystal model of only two slip systems! The following discussion should also serve, therefore, to explain the points made in the Introduction concerning the limitations of rate independent plasticity.

2.3.2. Uniqueness of slip mode. Hill and Rice [9] have shown that under conditions where the full set of deformation or stress rates are specified, sufficient conditions for slip mode uniqueness are that a matrix **g** or a matrix **k** be positive definite. When **D** is specified **g** must be positive definite where

$$g_{\alpha\beta} = h_{\alpha\beta} + \mathbf{P}^{(\alpha)}:\mathbf{L}:\mathbf{P}^{(\alpha)}:\mathbf{P}^{(\beta)} \tag{2.32}$$

whereas when the stress rate (i.e. $\overset{\nabla}{\boldsymbol{\tau}}$) is specified **k** must be positive definite where

$$k_{\alpha\beta} = h_{\alpha\beta} - \mathbf{P}^{(\alpha)}:\boldsymbol{\beta}^{(\beta)} - \boldsymbol{\beta}^{(\alpha)}:\mathbf{L}^{-1}:\boldsymbol{\beta}^{(\beta)}. \tag{2.33}$$

For the crystal model considered here

$$g_{\alpha\beta} = h_{\alpha\beta} - (\sigma/2)\cos 2\phi + G, \quad \alpha = \beta \tag{2.34$_1$}$$

$$g_{\alpha\beta} = h_{\alpha\beta} + (\sigma/2)\cos 2\phi - G\cos 4\phi, \quad \alpha \neq \beta \tag{2.34$_2$}$$

and

$$k_{\alpha\beta} = h_{\alpha\beta} + (\sigma/2)\cos 2\phi + 0(\sigma^2/G), \quad \alpha = \beta \tag{2.35$_1$}$$

$$k_{\alpha\beta} = h_{\alpha\beta} - (\sigma/2)\cos 2\phi + 0(\sigma^2/G), \quad \alpha \neq \beta. \tag{2.35$_2$}$$

The last terms of order σ^2/G in **k** can be dropped from consideration if $\sigma/G \ll 1$.

To model an f.c.c. crystal we take $\phi = 30°$ whereby $\cos 4\phi = -0.5$. Then **g** is positive definite so long as σ and the $h_{\alpha\beta}$ are much smaller in magnitude than G. This is the case for most values of ϕ with the notable exception of $\phi = 45°$ and $\cos 4\phi = -1$. In this degenerate case, the normals, in stress space, to the two yield planes are parallel and there is no yield vertex.

The situation for **k** is more difficult to state in general. However, if we take $h_{11} = h_{22} = h$ and $h_{12} = h_{21} = h_1$, it is easy to see that **k** is positive definite if and only if

$$h - h_1 + \sigma \cos 2\phi > 0 \tag{2.36}$$

or if $h_1 = qh$ as before

$$\cos 2\phi > (h/\sigma)(q-1). \tag{2.37}$$

As noted by Peirce *et al.* [1], this is effectively the condition that determines the sign of μ, the incremental shear modulus (cf. 2.31_2). To see how severe this restriction is we again take $\phi = 30°$ and recall from the discussion of Section 2.2 that q is expected to lie in the range $1 \le q \le 1.4$. If $q = 1.4$ the uniqueness condition is $h/\sigma < 1.25$ or since $\sigma \simeq 2.3\tau$, where τ is the resolved shear stress on either slip system, $h/\tau < 2.9$. The number of cases where this restriction would fail are indeed numerous; for many ductile metals, for example, the condition would fail in the first 1 to 2% strain when the flow stress is low and the strain hardening rates are high. The importance of latent hardening is again made clear if an orientation corresponding to $\phi > 45°$ is considered. For such cases $\cos 2\phi < 0$ and unless $q < 1$ uniqueness of the slip mode under prescribed stressing is never guaranteed.

While there is no direct connection between lack of uniqueness of slip mode under prescribed stressing and uniqueness of solutions of mixed boundary value problems of the sort considered here, the above discussion does illustrate just how precarious is the stability of the rate independent crystal. Indeed, with $\phi = 30°$ Peirce *et al.* [1] have shown that loss of uniqueness of the boundary value problem with prescribed all around displacements (via a shear band mode) occurs slightly before **k** ceases to be positive definite. By way of contrast our rate dependent material description does not suffer from such uniqueness limitations. There is, in fact, no division of slip systems into "active" and "inactive" sets; instead all slip systems are "active" with the slipping rate on each determined uniquely by the stress state as by (2.17).

2.3.3. Bifurcation results. Peirce *et al.* [1] have discussed the bifurcation problem as it pertains to this model in some detail. The present discussion is confined to shear bands and extends their discussion to include crystal geometries where $\phi > 45°$.

In the rate independent model shear bands become possible when h/σ falls to a critical value. For a band to form on a plane with unit normal (n_1, n_2), equilibrium and compatibility require that

$$(\mu - \sigma/2)n_1^4 + 2(2\mu^* - \mu)n_1^2 n_2^2 + (\mu + \sigma/2)n_2^4 = 0. \tag{2.38}$$

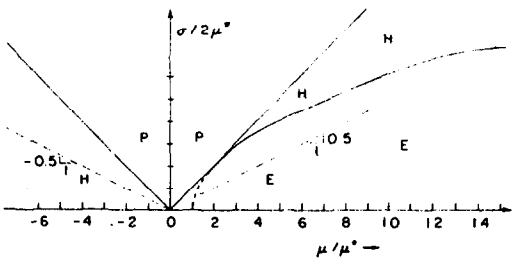

Fig. 5. Elliptic (E), hyperbolic (H) and parabolic (P) regimes in plane strain as determined by equation (2.38). Typically when $\phi = 30°$ the trajectory in this parameter space is along a line of slope 0.5; when $\phi = 60°$ the trajectory eventually falls on a line of slope -0.5.

The governing equations are elliptic, parabolic, or hyperbolic according as (2.38) admits 0, 2 or 4 real solutions for n_2/n_1; reaching the critical value for h/σ corresponds to crossing from the elliptic into the hyperbolic (H) or parabolic (P) regime.

These bifurcation results are summarized schematically in Fig. 5. The parameters chosen, $\sigma/2\mu^*$ and μ/μ^*, evolve with strain according to the strain hardening law specified for the material; as long as h and q are positive, however, $\sigma/2\mu^* > 0$.

For our crystal model the coordinates of Fig. 5 are expressed as

$$\mu/\mu^* = \frac{[(1-q) + (\tau/h)\cot 2\phi]\tan^2 2\phi}{(1+q)} \tag{2.39_1}$$

and

$$\sigma/2\mu^* = \frac{(\tau/h)\sin 2\phi}{(1+q)} \tag{2.39_2}$$

where τ ($=\frac{1}{2}\sigma \sin 2\phi$) is the resolved shear stress on either slip system in the (uniform) pre-bifurcation state. The two types of calculations discussed in this paper pertain to $\phi = 30°$ and $\phi = 60°$; these are analyzed in turn.

$\phi = 30°$. Suppose first that the hardening is isotropic and $q = 1$. Then $\mu/\mu^* > 1$ and $(\sigma/2\mu^*)/(\mu/\mu^*) = 0.5$. Thus as σ and τ increase and h decreases with strain the trajectory in the parameter space of the bifurcation figure, Fig. 5, is along a straight line of slope 0.5. Initially the state is elliptic but eventually meets and crosses the E–H boundary. This case was discussed by Asaro [12] and Peirce *et al.* [1]. At the E–H boundary there are two coincident real characteristics and the angle they make with the tensile axis, θ, is around $\theta \simeq 38°$–$40°$. Since τ is rising with strain and h is falling, this point is reached as soon as h/τ *falls* to a critically low value. It is instructive to study Fig. 6 which illustrates some important kinematical features of shear bands aligned along such characteristics.

Shear bands are characterized by double slip but with a clear dominance of slip in one system or the other. For the shear band mode, the ratio of excess slip on the conjugate system to that on the primary system is given by

$$\frac{\Delta\gamma^{(c)}}{\Delta\gamma^{(p)}} = \frac{\sin 2(\theta - \phi)}{\sin 2(\theta + \phi)}. \tag{2.40}$$

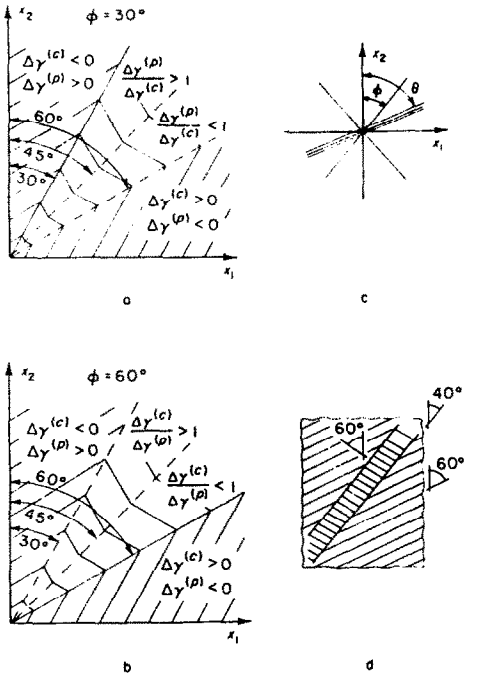

Fig. 6. Kinematics of real characteristics for the cases where $\phi = 30°$ (a) and $\phi = 60°$ (b). Only the upper right-hand quadrant of the crystal is shown—in this quadrant the primary slip system is oriented at $\phi = 30°$ in (a) and $\phi = 60°$ in (b). $\Delta\gamma^{(p)}$ and $\Delta\gamma^{(c)}$ are the excess shear strains on the primary and conjugate slip systems associated with shear bands. The signs and relative magnitudes of the $\Delta\gamma$'s are marked for possible shear band orientations. (d) A schematic of the slip line pattern associated with a "band of secondary slip" as implied by the analysis of (b).

Here Δ represents a jump in a quantity from the (homogeneous) prebifurcation state. For this case when $\phi = 30°$, Fig. 6(a) shows that when $30° < \theta < 45°$ the bands are dominated by primary slip. Thus the bifurcation picture is that when h/σ falls to the critical value (i.e. the E–H boundary is reached) shear bands of orientation $\theta = 30°$–$40°$ become possible—these bands are dominated by primary slip. For other values of q the situation is quite similar as long as ellipticity is lost at the E–H boundary. The bands still form initially on characteristics with $\theta = 38°$–$40°$ and are thus dominated by primary slip. On the other hand when q and h/σ are large enough for ellipticity to be lost by entry into the parabolic regime, the shear band mode only involves continued positive slipping on one system.

What is important to note is that only certain shear band orientations are consistent with positive slip activity on both slip systems; this is also indicated in Fig. 6. This range of orientations includes the critical orientation at the E–H boundary but not the orientation associated with the critical mode at the parabolic boundary. Since the bifurcation analysis assumes double slip it is necessary that the total bifurcation mode be so characterized. The total bifurcation mode necessarily consists of a linear combination of the shear band mode and the homogeneous pre-bifurcation solution (see Hutchinson [29]). When there is positive slip activity on both systems in the band, this combination gives neutral loading outside the band (incipient elastic unloading) along with positive slip activity on both systems in the band. This clearly tends to focus further deformation in the band. On the other hand when the shear band mode involves negative slip on one system in the band, the total bifurcation mode will involve single slip in the band and continued double slip outside the band. The stiffening of the band (relative to the material outside the band) associated with this mode of deformation promotes patchy slip behavior as discussed by Peirce *et al.* [1].

$\phi = 60°$. Figure 6(b) shows the corresponding kinematical picture for the case where $\phi = 60°$. The relative position of primary slip dominated and conjugate slip dominated bands about $\theta = 45°$ is reversed from the previous case where $\phi = 30°$. It is then important to see where the most favored characteristics lie.

If we again take $q = 1$, $\mu/\mu^* < 0$ and $(\sigma/2\mu^*)/(\mu/\mu^*) = -0.5$; that is, the trajectory in the parameter space of Fig. 5 is along a line of slope -0.5 lying entirely in H. Table 1 lists some of the characteristic angles computed from (2.38) along this line. What is important is that one characteristic crosses the angle $\theta \geq 30°$ long before the other reaches $\theta \leq 60°$. In fact as $\mu/\mu^* \to -\infty$, $\theta_1 \to 45°$ and $\theta_2 \to 60°$ so that the second characteristic *never* enters the region $30° \leq \theta \leq 60°$ which is associated with active double slip. The characteristic with an orientation $30° \leq \theta \leq 45°$ produces bands of localized *conjugate* slip and, because the orientation of this band obviously puts it much closer to the primary slip system, it seems appropriate to refer to it as a "band of secondary slip". The sort of "slip line pattern" to be expected from this mode is sketched in Fig. 6(d)—this has a rough similarity to that shown earlier in Fig. 1.

Our calculations for $\phi = 60°$, described next, used the following hardening law

$$h(\gamma) = h_0 \operatorname{sech}^2\left[\frac{h_0\gamma}{\tau_s - \tau_0}\right] \tag{2.41}$$

with $h_0 = 40\tau_0$ and $\tau_s = 1.2\tau_0$. For this case $\tau_0/h = (1/160)[e^{200\gamma} + e^{-200\gamma}]$. For q in the range $0.7 < q < 1.2$ for example, it turns out that (μ/μ^*) becomes less than -10 and $(\sigma/2\mu^*)/(\mu/\mu^*)$ falls on a line of slope -0.5 after only about 2% glide strain. The expectation then,

Table 1. Characteristic angles in the hyperbolic regime where $\mu < 0$. The characteristics are for the case $(\sigma/2\mu^*)/(\mu/\mu^*) = -0.5$

(μ/μ^*)	$\sigma/2\mu^*$	θ_1 (in degrees)	θ_2 (in degrees)
−0.1	0.05	10.7	83.77
−1.0	0.5	26.81	73.73
−2.0	1.0	32.13	70.07
−4.0	2.0	36.57	66.81
−10.0	5.0	40.68	63.61

is that conjugate bands with orientation $30° \leq \theta \leq 40°$ become possible soon after initial yield. The bands may approach $\theta \simeq 45°$ after further strain. If the material were more strongly strain hardening the strains where this would begin would increase, but the kinematical patterns would be similar. Exactly how the bands develop, however, depends also on the material's rate sensitivity and must be determined by the calculations. It is useful in any case to be able to anticipate some of the possible general features in order to develop a suitable and accurate finite element model.

3. NUMERICAL CALCULATIONS

3.1. *Numerical method*

Except for the crystal constitutive relation employed, the numerical method used in the present study is identical to that described in Peirce *et al.* [1]. As in that study the calculations are carried out using the plane strain crystal model depicted in Fig. 2. The initial length of the crystal is $2L_0$ and its initial thickness is $2(h_0 + \Delta h_0)$ where $2h_0$ is the average thickness and $2\Delta h_0$ is the initial thickness inhomogeneity. Prior to the onset of deformation the slip systems are taken to be symmetrically oriented about the tensile axis. The end-displacement rate of the crystal is prescribed and the deformation history calculated in a linear incremental fashion.

In the initial unstressed state of the crystal, material points are identified by their Cartesian coordinates x^i; these coordinates may be viewed as inscribed on the body in the undeformed configuration. As the material deforms, the coordinate net is convected with it. The displacement components u^i on the reference base vectors determine the components of the Lagrangian strain tensor via

$$\eta_{ij} = \tfrac{1}{2}(u_{i,j} + u_{j,i} + u^k_{,i} u_{k,j}), \tag{3.1}$$

where a comma denotes covariant differentiation in the reference coordinate system. In general, the indices in (3.1) range from 1 to 3, but they only range from 1 to 2 in the present plane strain problem, both here and subsequently.

The contravariant components of Kirchhoff stress on the convected deformed coordinates are denoted τ^{ij}. On an element of surface whose normal in the reference configuration had covariant components n_i, the contravariant components of nominal traction on the reference coordinates are

$$T^j = n_i(\tau^{ij} + \tau^{ik} u^j_{,k}). \tag{3.2}$$

The principle of virtual work may now be written as

$$\int_V \tau^{ij} \delta\eta_{ij}\, dV = \int_S T^i \delta u_i\, dS \tag{3.3}$$

where V and S denote volume and surface in the undeformed reference configuration.

As in Peirce *et al.* [1], the deformations calculated here are restricted to be symmetric about the mid-planes of the crystal. Because of this symmetry, only one (here, the first) quadrant of the crystal needs to be analyzed numerically. At a given time t, the boundary conditions on the quadrant analyzed numerically are

$$\begin{aligned} &\dot{u}^1 = 0, \quad \dot{T}^2 = 0 \quad \text{on} \quad x^1 = 0 \\ &\dot{u}^2 = 0, \quad \dot{T}^1 = 0 \quad \text{on} \quad x^2 = 0 \\ &\dot{T}^1 = \dot{T}^2 = 0 \quad \text{on} \quad x^1 = h_0 + \Delta h_0 \\ &\dot{u}^2 = \dot{U}, \quad \dot{T}^1 = 0 \quad \text{on} \quad x^2 = L_0 \end{aligned} \tag{3.4}$$

The boundary conditions (3.4) are such that the deformation state for a perfect crystal ($\Delta h_0 = 0$) is one of homogeneous symmetric double slip; for an imperfect crystal ($\Delta h_0 \neq 0$) the deformations are inhomogeneous from the outset. The initial thickness imperfection Δh_0 follows that of Tvergaard *et al.* [19], and is given by

$$\Delta h_0 = h_0 \left[-\xi_1 \cos\left(\frac{\pi x^2}{L_0}\right) + \xi_2 \cos\left(\frac{p x^2}{L_0}\right) \right]. \tag{3.5}$$

Here ξ_1 and ξ_2 are prescribed amplitudes and $p > 1$ is an integer wavenumber.

In the linear incremental problem, suppose a current state of approximate equilibrium to be known at time t; to determine the equations for the field quantity rates, equation (3.3) is expanded in a Taylor series about the time t to yield

$$\begin{aligned} &\dot{}\left[\int_V [\tau^{ij} \delta\eta_{ij} + \tau^{ij} \dot{u}_{k,i} \delta u^k_{,j}]\, dV \right] \\ &= \dot{}\left[\int_S \dot{T}^i \delta u_i\, dS \right] \\ &\qquad + \left[\int_S T^i \delta u_i\, dS - \int_V \tau^{ij} \delta\eta_{ij}\, dV \right]. \end{aligned} \tag{3.6}$$

The last term on the right of (3.6) serves as an equilibrium correction if equilibrium in the current state is only approximate.

The contravariant components of the convected derivative of Kirchhoff stress, $\dot{\tau}^{ij}$, appearing in (3.6) are related to Jaumann stress rate components in the constitutive relations (2.14) via

$$\dot{\tau}^{ij} = \overset{\circ}{\tau}{}^{ij} - \bar{g}^{ik} \tau^{jl} \dot{\eta}_{kl} - \bar{g}^{jk} \tau^{il} \dot{\eta}_{kl}. \tag{3.7}$$

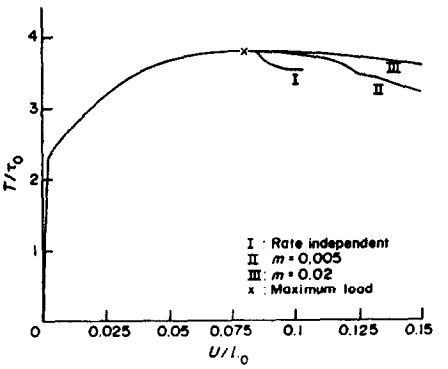

Fig. 7. Normalized load vs end displacement for the case where $\phi = 30°$ and $q = 1$. Curves are shown for three values of m, $m = 0$, 0.005 and 0.02.

Employing (2.14) in conjunction with (3.7) directly in the incremental principle of virtual work leads to an explicit Euler time integration scheme in which the finite element stiffness matrix is derived from the elasticity tensor **L**. In the present context, this approach requires extremely small time steps to ensure numerical stability. The maximum allowable time step is inversely related to the relevant material stiffness (Cormeau [20]). We will employ a method in which an estimate is made of the change in shear rates, $\dot{\gamma}^{(\alpha)}$, during the current time increment. This leads to an expression for a tangent stiffness which is considerably reduced from the elastic stiffness, and which leads to improved numerical stability. This numerical procedure falls into the class of forward gradient methods (Shih *et al.* [21]; Willam [22]; Zirin and Krempl [23] and Little *et al.* [24]). A general discussion of this numerical procedure is given in Peirce *et al.* [25] for a variety of continuum constitutive relations. Here we will focus on those aspects particular to the single crystal context.

The slip increment on system α at time t is defined by

$$\Delta\gamma^{(\alpha)} = \gamma^{(\alpha)}(t+\Delta t) - \gamma^{(\alpha)}(t). \tag{3.8}$$

A linear interpolation is employed within the time increment to obtain

$$\Delta\gamma^{(\alpha)} = [(1-\theta)\dot{\gamma}^{(\alpha)}(t) + \theta\dot{\gamma}^{(\alpha)}(t+\Delta t)]\Delta t \tag{3.9}$$

where Δt is the time increment. The parameter θ ranges from 0 to 1; $\theta = 0$ corresponds to the simplest Euler integration procedure. To approximate the last term in (3.9), we employ a Taylor expansion of (2.17)

$$\dot{\gamma}^{(\alpha)}(t+\Delta t) = \dot{\gamma}^{(\alpha)}(t) + \left(\frac{\partial\dot{\gamma}^{(\alpha)}}{\partial\tau^{(\alpha)}}\right)_t \Delta\tau^{(\alpha)} + \left(\frac{\partial\dot{\gamma}^{(\alpha)}}{\partial g^{(\alpha)}}\right)_t \Delta g^{(\alpha)}$$
$$= \operatorname{sgn}(\tau^{(\alpha)})\dot{a}^{(\alpha)}\left(\left|\frac{\tau^{(\alpha)}}{g^{(\alpha)}}\right|\right)^{1/m}\left[1 + \frac{1}{m}\left(\frac{\Delta\tau^{(\alpha)}}{\tau^{(\alpha)}} - \frac{\Delta g^{(\alpha)}}{g^{(\alpha)}}\right)\right] \tag{3.10}$$

where sgn( ) denotes "the sign of," $\Delta\tau^{(\alpha)} = \dot{\tau}^{(\alpha)}\Delta t$ and $\Delta g^{(\alpha)} = \dot{g}^{(\alpha)}\Delta t$. Using $\dot{\tau}^{(\alpha)} = \mathbf{R}^{(\alpha)}:\mathbf{D}^*$, where $\mathbf{R}^{(\alpha)}$ is given by (2.15), and (2.17) in (3.10) and (3.9), we obtain

$$\Delta\gamma^{(\alpha)} = \dot{\gamma}_t^{(\alpha)}\Delta t + \frac{\theta\Delta t\dot{\gamma}_t^{(\alpha)}}{m\tau^{(\alpha)}}[\mathbf{R}^{(\alpha)}:\mathbf{D}] - \frac{\theta\Delta t\dot{\gamma}_t^{(\alpha)}}{m\tau^{(\alpha)}}\sum_\beta \mathbf{R}^{(\alpha)}:\mathbf{P}^{(\beta)}\dot{\gamma}^{(\beta)} - \frac{\theta\Delta t\dot{\gamma}_t^{(\alpha)}}{mg^{(\alpha)}}\sum_\beta h_{\alpha\beta}\operatorname{sgn}(\dot{\gamma}^{(\beta)})\dot{\gamma}^{(\beta)}. \tag{3.11}$$

This equation may be written concisely as

$$\sum_\beta N_{\alpha\beta}\Delta\gamma^{(\beta)} = (\dot{\gamma}_t^{(\alpha)} + \mathbf{Q}^{(\alpha)}:\mathbf{D})\Delta t \tag{3.12}$$

where

$$\dot{\gamma}_t^{(\alpha)} = \dot{a}^{(\alpha)}\frac{\tau^{(\alpha)}}{g^{(\alpha)}}\left(\left|\frac{\tau^{(\alpha)}}{g^{(\alpha)}}\right|\right)^{1/m-1} \tag{3.13}$$

$$\mathbf{Q}^{(\alpha)} = \left(\frac{\theta\Delta t\dot{\gamma}_t^{(\alpha)}}{m\tau^{(\alpha)}}\right)\mathbf{R}^{(\alpha)} \tag{3.14}$$

and

$$N_{\alpha\beta} = \delta_{\alpha\beta} + \left(\frac{\theta\Delta t\dot{\gamma}_t^{(\alpha)}}{m}\right) \times \left[\frac{\mathbf{R}^{(\alpha)}:\mathbf{P}^{(\beta)}}{\tau^{(\alpha)}} + \operatorname{sgn}(\tau^{(\beta)})\frac{h_{\alpha\beta}}{g^{(\alpha)}}\right]. \tag{3.15}$$

Here we have identified $\operatorname{sgn}(\dot{\gamma}^{(\beta)})$ with $\operatorname{sgn}(\dot{\gamma}_t^{(\beta)}) = \operatorname{sgn}(\tau^{(\beta)})$. For fixed θ and fixed rate sensitivity m, $N_{\alpha\beta}$ is invertible for a sufficiently small time increment Δt. This contrasts with the rate independent case where $N_{\alpha\beta}$ is not necessarily invertible. Indeed, in the rate independent limit [$m \to 0$, fixed $(\theta\Delta t)$], $mN_{\alpha\beta}$ in (3.15) approaches its rate independent counterpart. However, for any $m > 0$ a sufficiently small time step can be chosen so that $N_{\alpha\beta}$ is invertible. Thus, for rate dependent material behavior a unique set of slip rates is always available for any prescribed strain rate. We also note that in general $N_{\alpha\beta} \neq N_{\beta\alpha}$.

Denote the inverse of $N_{\alpha\beta}$ by $M_{\alpha\beta}$. Then inverting (3.12) leads to

$$\Delta\gamma^{(\alpha)} = (\hat{f}^{(\alpha)} + \hat{\mathbf{F}}^{(\alpha)}:\mathbf{D})\Delta t \tag{3.16}$$

where

$$\hat{f}^{(\alpha)} = \sum_\beta M_{\alpha\beta}\dot{\gamma}_t^{(\alpha)} \quad \text{and} \quad \hat{\mathbf{F}}^{(\alpha)} = \sum_\beta M_{\alpha\beta}\mathbf{Q}^{(\beta)}. \tag{3.17}$$

Equation (3.16) now allows (2.14) to be rewritten as

$$\overset{\nabla}{\boldsymbol{\tau}} = \mathbf{C}:\mathbf{D} - \sum_\alpha \mathbf{R}^{(\alpha)}\hat{f}^{(\alpha)} \tag{3.18}$$

where the moduli **C** are defined by

$$\mathbf{C} = \mathbf{L} - \sum_\alpha \mathbf{R}^{(\alpha)}\hat{\mathbf{F}}^{(\alpha)}. \tag{3.19}$$

Note that, since $N_{\alpha\beta}$ is not in general symmetric, the moduli **C** will not in general possess the pairwise symmetry that existence of an elastic strain energy density implies for **L**. On the deformed convected coordinates, the component form of (3.18) is

$$\overset{\nabla}{\tau}{}^{ij} = C^{ijkl}\dot{\eta}_{kl} - \sum_\alpha \mathbf{R}^{(\alpha)ij}\hat{f}^{(\alpha)}. \tag{3.20}$$

Many of the tensors which comprise the incremental moduli (3.19) depend on the current material and lattice geometries. It is important that updating which makes use of these tensors be performed before the current coordinate systems are redefined. One may begin by calculating the slip increments $\dot{\gamma}^{(\alpha)}$ directly from (3.16). These in turn allow updating of the $g^{(\alpha)}$ by (2.20). The stress state is incremented by using (3.7) and (3.18).

Once slips and stresses have been updated, the geometry is next. The new deformation gradient **F** follows immediately from the displacements; its plastic part $\mathbf{F}^p$ is updated via (2.4). The new $\mathbf{F}^*$ is then just $\mathbf{F}\cdot\mathbf{F}^{p-1}$. Knowing $\mathbf{F}^*$, one may recalculate $\mathbf{P}^{(\alpha)}$, $\mathbf{W}^{(\alpha)}$, $\boldsymbol{\beta}^{(\alpha)}$, and $\mathbf{R}^{(\alpha)}$. The resolved shear stresses $\tau^{(\alpha)}$ also follow. A new current state is thus defined, and one may solve for a new set of incremental displacements based on the new incremental constitutive law (3.18).

3.2. Numerical results

The finite element computations reported on here were carried out using Asaro's [12] plane model depicted in Fig. 2. Analyses of two crystal geometries were carried out. In each case the value of the reference strain rate $\dot{a}^{(\alpha)}$ in (2.17) is given by $\dot{a}^{(\alpha)} = \dot{a}_0$, a constant for all slip systems α. The prescribed displacement rate $\dot{U}$ is taken to be $\dot{U} = \dot{a}_0 L_0$. Due to the nature of the constitutive relation, the results depend primarily on the ratio $\dot{U}/\dot{a}_0 L_0$ which here is prescribed to be unity. A slight dependence of the results on the magnitude of $\dot{a}_0$ (keeping $\dot{U}/\dot{a}_0 L_0$ fixed) arises from the crystal elasticity. In our computations the material time constant $\tau_0/E\dot{a}_0$ is always taken to be equal to unity.

In one case, we take $\phi = \psi = 30°$, as in Peirce *et al.* [1]. For an f.c.c. crystal this is the angle that the primary and conjugate slip directions would make with the stable ⟨112⟩ tensile direction. In these calculations, the material properties are taken to be identical to one of the cases considered in Peirce *et al.* [1] except, of course, that here we account for material strain rate sensitivity. In particular, we take $E = 1000\ \tau_0$, $\nu = 0.3$, and $\tau_s = 1.8\ \tau_0$, $h_0 = 8.9\ \tau_0$ in (2.23).

Calculations are carried out for various latent hardening ratios, q, to illustrate the dependence of patchy slip development on latent hardening ratio. For two cases, one with $q = 1$ (Taylor hardening) and the other with $q = 1.4$, we follow the crystal through the onset of necking and the development of shear bands.

In the other case we take $\phi = \psi = 60°$ to model a somewhat different sort of orientation and in particular one which can be used to model b.c.c. crystals as tested by Reid *et al.* [4]. Within the rate independent framework, this geometry gives rise to a quite different bifurcation behavior than does the f.c.c. geometry as discussed earlier in Section 2.3. As our numerical results will show, the development of localized plastic flow in this calculation is also quite different from that in the f.c.c. model crystals. The specific material parameters employed here are $E = 1000\ \tau_0$, $\nu = 0.3$, $\tau_s = 1.2\ \tau_0$, $h_0 = 40\ \tau_0$, $\dot{a}_0 = 0.001$ and various values of q, $q = 0.75$, 0.9, 1.1 and m, $m = 0.005$ and 0.002. The material properties were chosen to give a resolved shear stress–shear strain curve with high initial hardening that rapidly saturates. As in the f.c.c. simulations we take $\tau_0/E\dot{a}_0 = 1$ and $\dot{U}/\dot{a}_0 L_0 = 1$.

3.2.1. Results for f.c.c. crystal simulations. The initial aspect ratio of the crystals considered here is $L_0/h_0 = 3$ and the initial thickness imperfection is given by (4.5), with $\xi_1 = 0.42 \times 10^{-2}$, $\xi_2 = 0.24 \times 10^{-2}$, and a wave number $p = 2$.

The finite element discretization takes the form of 768 quadrilaterals within the first quadrant of Fig. 2. Each quadrilateral consists of four constant strain triangles. These triangles are not shown in figures like Fig. 8 which presents deformed finite element meshes for a crystal with rate sensitivity $m = 0.005$. The complete crystal is shown, even though the assumed symmetry allows the calculations to be performed for the first quadrant only, with the boundary conditions (3.4).

The normalized extension in Fig. 8(a) is $U/L_0 = 0.1$, and the deformation pattern is quite uniform. The slightest hint of shear bands crossing at the specimen center is evident in Fig. 8(b), where $U/L_0 = 0.12$, but they are developed most fully at $U/L_0 = 0.15$. The corresponding mesh is shown in Fig. 8(c).

It is interesting to compare Fig. 7 with Fig. 8, where the curve labeled II gives the load–extension plot for the crystal of Fig. 8. Here, τ_0 normalizes the load per unit initial area T, given by

$$T = \frac{1}{2(h_0 + \Delta h_0)} \int_{-(h_0 + \Delta h_0)}^{h_0 + \Delta h_0} T^2(L_0, x^1)\, dx^1. \quad (3.21)$$

Note the smoothness of curve II up to $U/L_0 = 0.12$, several percent strain beyond the maximum load at $U/L_0 = 0.08$. There is a modestly abrupt load drop, however, at $U/L_0 = 0.12$, and as shear accumulates in the bands noted in Fig. 8(c), the load continues to fall. Although a marked decrease in load is associated with shear band formation in the crystal of Fig. 8, an even more abrupt drop takes place in curve I. This curve which is taken from the results of Peirce *et al.* [1] gives the load–extension data for a crystal identical to that in Fig. 8, except that it is rate independent. The crystal corresponding to curve I begins to form shear bands within a half percent strain of maximum load, and these bands develop fully with little additional extension. Nevertheless, the small rate sensitivity in curve II delays shear band initiation significantly, and prolongs development of the ultimate shear band pattern. The experimental work of Chang and Asaro [16] on symmetrically oriented aluminum alloy crystals led to

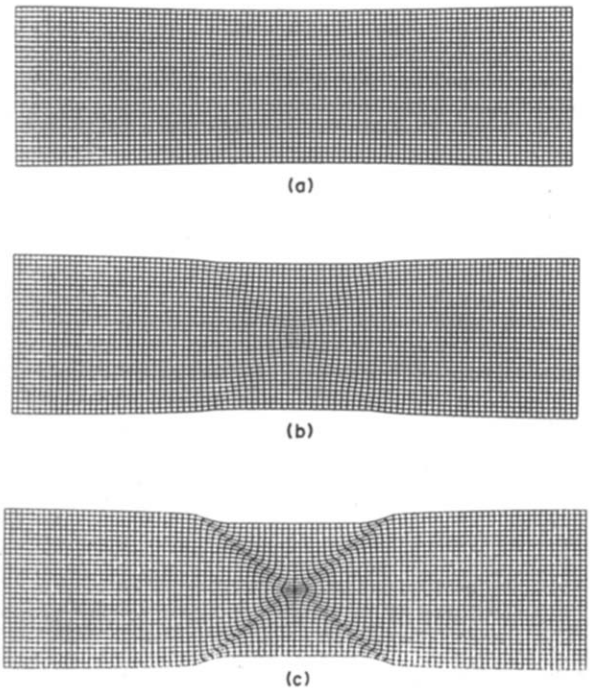

Fig. 8. Deformed finite element meshes for the case where $\phi = 30°$, $q = 1$ and $m = 0.005$. (a) $U/L_0 = 0.10$, (b) $U/L_0 = 0.12$, and (c) $U/L_0 = 0.15$.

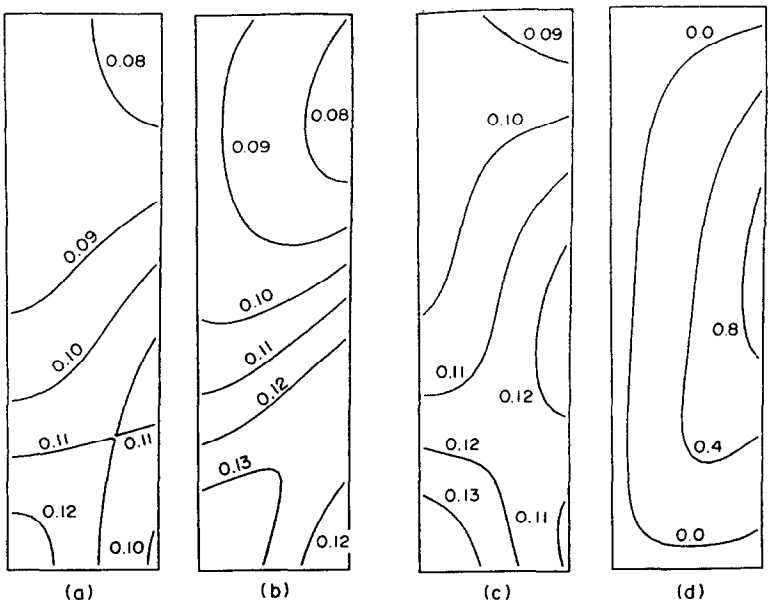

Fig. 9. Contours of strain and lattice rotation in one quadrant of the deformed crystal shown in Fig. 8(a). (a) Contours of constant maximum principal logarithmic strain; (b) contours of constant glide strain on the primary slip system; (c) contours of constant glide strain on the conjugate slip system; and (d) contours of constant rotation (in degrees) of the primary slip direction away from the tensile axis.

load–extension plots in qualitative and quantitative agreement with curve II here. The effect of an increase in rate sensitivity to $m = 0.02$ is indicated by curve III, where the load falls very slowly from its maximum. In fact, over the extension range calculated, no shear bands were observed in this computation and the load–extension curve shows no discernible difference from that of an identical crystal without a thickness imperfection. Thus, while all the curves of Fig. 7 have a normalized maximum load of $T/\tau_0 = 3.78$ at a normalized extension of $U/L_0 = 0.08$, they differ markedly after maximum load.

A more quantitative picture of the development of localization in the case with $m = 0.005$ is furnished by Figs 9–11, where various contours are plotted within the first quadrant of the crystal. Figures 9(a) to 11(a) show contours of constant maximum principal logarithmic strain. Figures 9(b) to 11(b) and 9(c) to 11(c)

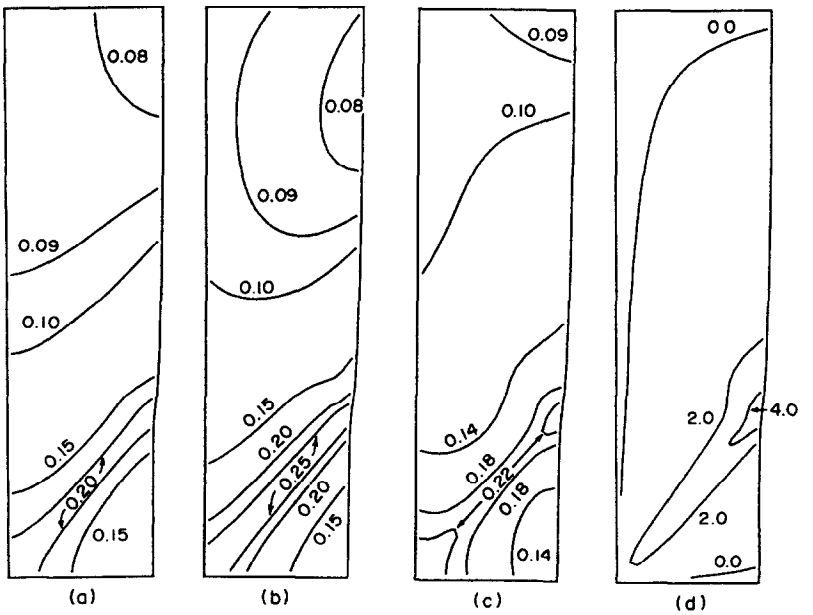

Fig. 10. Contours of strain and lattice rotation in one quadrant of the deformed crystal shown in Fig. 8(b). (a) Contours of constant maximum principal logarithmic strain; (b) contours of constant glide strain on the primary slip system; (c) contours of constant glide strain on the conjugate slip system; and (d) contours of constant rotation (in degrees) of the primary slip direction away from the tensile axis.

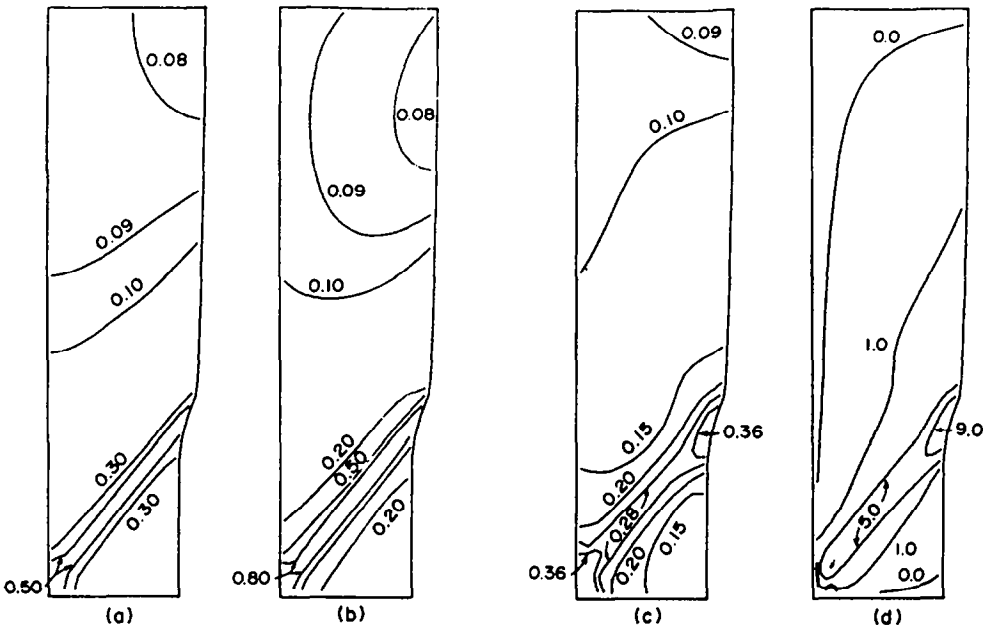

Fig. 11. Contours of strain and lattice rotation in one quadrant of the deformed crystal shown in Fig. 8(c). (a) Contours of constant maximum principal logarithmic strain; (b) contours of constant glide strain on the primary slip system; (c) contours of constant glide strain on the conjugate slip system; and (d) contours of constant rotation (in degrees) of the primary slip direction away from the tensile axis.

depict similar contour plots of shear strain on the primary and conjugate slip systems, respectively. The contours in Figs 9(d)–11(d) correspond to lattice rotation. The values shown correspond to the rotation in degrees of the primary slip system away from its initial orientation of 30° from the tensile axis; positive values show clockwise rotation. Since elastic strains are small, the rotation of the primary slip system is essentially equivalent to the rotation of the entire lattice.

Figure 9 corresponds to Fig. 8(a), where $U/L_0 = 0.1$. While the strain pattern is slightly nonuniform, Fig. 9(a) shows the inhomogeneity to correspond to the early stages of necking, since the highest strains are at the specimen center. This is also borne out by Figs 9(b) and 9(c). In these figures, note additionally that primary and conjugate slipping are equal at the left boundary where the symmetry condition holds; at the free surface on the right, the initial thickness imperfection has led to a slight preference for conjugate slipping. This preference is consistent with the higher rotation of the primary slip system near the free surface in Fig. 9(d). The consequent geometrical softening of the primary slip system can play an important role in shear band formation, particularly in deeply necked crystals as shown earlier by Peirce *et al.* [1].

While not discernible in Fig. 9, a shear band pattern is evident in Fig. 10, which shows contour plots at $U/L_0 = 0.12$. In Fig. 10(a)–(c), note how little additional straining has occurred in the upper portion of the specimen as compared to Fig. 9. Nearer the specimen center, however, strain has begun to concentrate in a well-defined band, as evidenced by the 0.2 contour in Fig. 10(a). Figure 10(b) and (c) also show this pattern, but the shear strain is greater in Fig. 10(b), and in fact well in excess of 0.25. This is consistent with the orientation of the shear band near the primary rather than the conjugate slip system, the activity of which (see Fig. 10(c)) is nevertheless prominent. The lattice continues to rotate, however, and Fig. 10(d) indicates substantial geometrical softening of the primary slip system, in accord with the excess straining evident in Fig. 10(b).

The shear band has fully developed in Fig. 11. The strains in Fig. 11(a) exceed 0.5 in the shear band, even though the overall normalized extension is only $U/L_0 = 0.15$. Virtually all the continuing deformation is concentrating in the narrow shear band region. Similar conclusions may be drawn from Fig. 11(b), where primary shear strains exceed 0.8 within the band. Figure 11(c) shows the lesser strains on the conjugate slip system. Conjugate slip activity is crucial to the shear band pattern, however, as Peirce *et al.* [1] {and the relation (2.40)} have demonstrated that the orientation of the shear band depends directly on the amount of conjugate slip therein. The shear band in Fig. 11 is 40° from the tensile axis, the same orientation as the rate independent results exhibit. Figure 11(d) shows rotations of the primary slip system greater than 9°, almost as great as that of the shear band itself.

A comparison of the rate independent calculations of Peirce *et al.* [1] with the present rate dependent calculations indicates then some important conclusions. At least for a relatively low hardening crystal such as the one modeled here by (2.23), rate sensitivity does not seem to affect greatly the actual shear band pattern. The rate independent crystal whose load curve is shown here in Fig. 7 is identical in all other respects to the rate

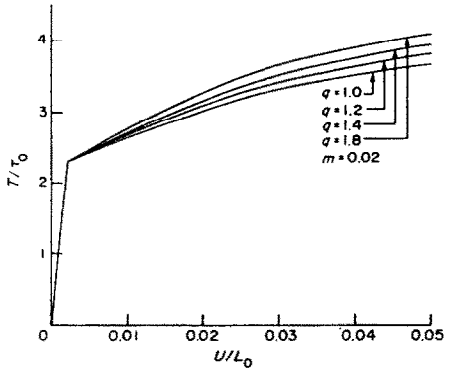

Fig. 12. Normalized load vs end displacement for $\phi = 30°$, $m = 0.02$ and for various latent hardening ratios, q.

dependent crystal. Both these crystals develop shear bands exhibiting a characteristic inclination of 40° to the tensile axis. Figure 7 indicates clearly, however, that even a rate sensitivity which has a small effect on the flow stress can delay shear band development significantly.

The smoothing effect of rate sensitivity noted in Fig. 7 has important consequences for another aspect of single crystal deformation, viz. the patchy slip patterns described by Peirce *et al.* [1]. When the latent hardening is sufficiently high, there is a constitutive nonuniqueness (2.36) and, in addition, the rate independent governing equations become parabolic. With the hardening law, (2.21) and (2.23), this prevented them from making calculations near initial yield when q was as small as 1.2. Yet it is precisely in the first few percent strain after initial yield that patches of slip arise.

The rate dependent constitutive law described in Section 2 has made finite element calculations with high values of q feasible. In particular, three high latent hardening crystal specimens were simulated here up to five percent extension. The strains developed are not high enough to cause shear bands, but patches of slip do arise at small strains.

The load–extension curves for these crystals are shown in Fig. 12, where q values of 1.2, 1.4, and 1.8 were used. The value $q = 1.0$ is also shown for comparison. All four curves are for crystals with $m = 0.02$. Note that even though a yield point per se does not exist in a rate sensitive material, the present constitutive law shows a very definite load at which plastic deformation is initiated, even on the scale of Fig. 12.

Contour plots analogous to Figs 9–11 are presented in Figs 13–15, which all correspond to normalized extensions of $U/L_0 = 0.05$. Figure 13 shows these plots for $q = 1.2$, corresponding to the second curve in Fig. 12. The strain pattern in Fig. 13(a) is quite uniform, with slight inhomogeneities arising at the free surface due to the initial thickness imperfection. The slip patterns of Figs 13(b) and (c) show similar effects of the initial thickness variation, while primary and conjugate slip seem to be roughly equal near the symmetry boundary. The conjugate slip concentration over most of the free surface, however, is more pronounced than the corresponding strain concentration in Fig. 13(a). The higher lattice rotations at the free surface in Fig. 13(d) are consistent with the conjugate slip pattern.

Figure 14 has corresponding contours for an identical crystal with $q = 1.4$. In Fig. 14(a), the small oblong regions at either end of the crystal accommodate the more severe development of patches in Figs 14(b) and (c). In Fig. 14(b), primary slip has a large valley spreading from the upper free surface and a marked peak in the left portion of the figure, as well as

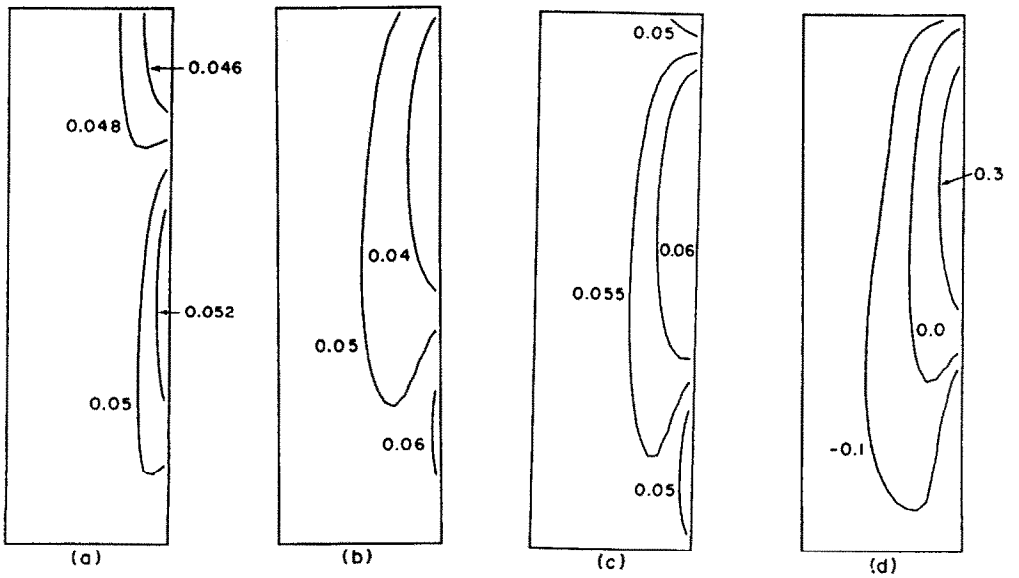

Fig. 13. Contours of strain and lattice rotation in one quadrant of the deformed crystal for the case where $\phi = 30°$, $q = 1.2$ and $m = 0.02$. These contours correspond to an end displacement of $U/L_0 = 0.05$. (a) Contours of constant maximum principal logarithmic strain; (b) contours of constant glide strain on the primary slip system; (c) contours of constant glide strain on the conjugate slip system; and (d) contours of constant rotation (in degrees) of the primary slip direction away from the tensile axis.

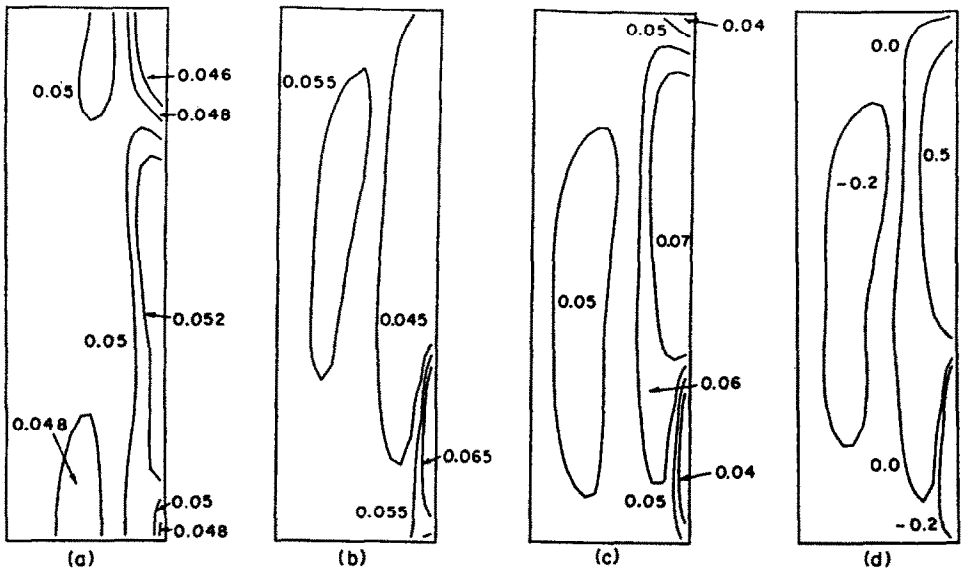

Fig. 14. Contours of strain and lattice rotation in one quadrant of the deformed crystal for the case where $\phi = 30°, q = 1.4$ and $m = 0.02$. These contours correspond to an end displacement of $U/L_0 = 0.05$. (a) Contours of constant maximum principal logarithmic strain; (b) contours of constant glide strain on the primary slip system; (c) contours of constant glide strain on the conjugate slip system; and (d) contours of constant rotation (in degrees) of the primary slip direction away from the tensile axis.

on the free surface nearer the specimen center. The conjugate slip pattern in Fig. 14(c) complements the primary slip configuration. The peak is now at the upper free surface, and the valleys are precisely where the primary shear strain peaks. As each half of the crystal has increased preference for single slip, the contours at either end of Fig. 14(a) indicate the strain inhomogeneities that arise as the overall tensile constraint comes into play. As before, the lattice rotations in Fig. 14(d) are in agreement with the nonuniform slip patterns.

The division of the crystal into two single slip regions acquires even more definition when $q = 1.8$. Contour plots for such a crystal are shown in Fig. 15. The strain pattern of Fig. 15(a) is a more pronounced version of Fig. 14(a). While the peaks and valleys are roughly in the same regions of the specimen, the strain patterns at the top and bottom of Fig. 15(a) suggest that the overall tensile constraint is more stringent here. This is borne out by Fig. 15(b) and (c), where the preference for single slip noted in Fig. 14 has also become more pronounced. Again the peaks and valleys occupy the same regions of

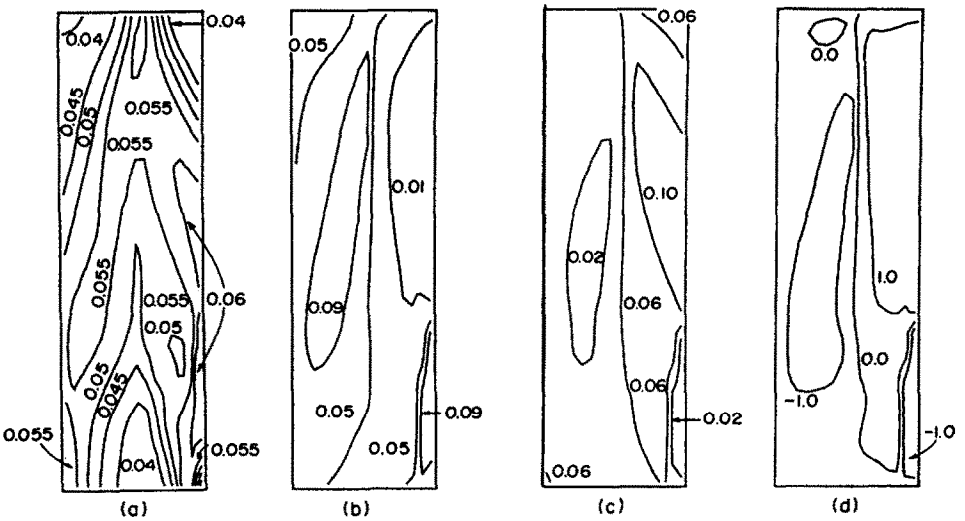

Fig. 15. Contours of strain and lattice rotation in one quadrant of the deformed crystal for the case where $\phi = 30°, q = 1.8$ and $m = 0.02$. These contours correspond to an end displacement of $U/L_0 = 0.05$. (a) Contours of constant maximum principal logarithmic strain; (b) contours of constant glide strain on the primary slip system; (c) contours of constant glide strain on the conjugate slip system; and (d) contours of constant rotation (in degrees) of the primary slip direction away from the tensile axis.

the specimen, but now virtually all the straining in a given region arises on a single slip system. The corresponding lattice rotations in Fig. 15(d), in excess of 1°, are not usually observed at these small strains; compare Fig. 9(d), for example.

The only crystal property that varies from Figs 13–15 is the latent hardening parameter q. It is not surprising that high values of q precipitate the nonuniform slip patterns which have been described above. When the initial imperfection leads a region of the crystal to begin plastic flow by single slip, the high latent hardening immediately inhibits the accumulation of any shear strain on the other system. The tensile constraints can overcome this tendency to some extent. Peirce *et al.* [1] noted that patches of primary and conjugate slip would alternate in narrow regions across the crystal to meet the boundary conditions. Here, the latent hardening is higher and the crystal is rate sensitive, so that the regions of single slip are broadened, and accommodation of the tensile constraints occurs entirely at $x^2 = 0$ and $x^2 = L_0$.

It is important to note that the calculations of Figs 13–15 are for a moderately rate sensitive crystal with $m = 0.02$. Similar calculations, not discussed here, show that the nonuniformities described above become more pronounced when $m = 0.005$. The rate sensitivity is still high enough, however, to split the crystal into two fairly distinct regions of single slip, rather than into the narrower patches noted by Peirce *et al.* [1].

The final f.c.c. simulation we discuss is based on a hardening law identical to the one used in the previous calculations [$\tau_s = 1.8\tau_0$, $h_0 = 8.9\tau_0$ in (2.23)] except that the rate sensitivity exponent m is taken as $m = 0.001$. The latent hardening ratio is prescribed to be $q = 1.4$ and we follow the deformations past the maximum load point through the onset of necking and the development of shear bands. The initial thickness imperfection is identical to the one employed in Figs 8–11, where $q = 1$. The load vs end-displacement curve is shown in Fig. 16. This load deflection curve does not exhibit the abrupt drop shown in Fig. 8 and, accordingly, there is a relatively gradual rotation of the crystal lattice in the shear band into a geometrically softer orientation. Figure 17 shows the deformed finite element mesh at the three stages of deformation marked on the load-end displacement curve of Fig. 16. In Fig. 17(a), the nonuniformity of deformation associated with patchy slip is visible in the deformed mesh. Subsequently a shear band does develop but it does not propagate across the gage.

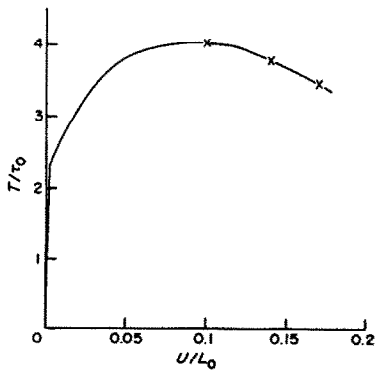

Fig. 16. Normalized load vs end displacement for the case where $\phi = 30°$, $q = 1.4$ and $m = 0.001$.

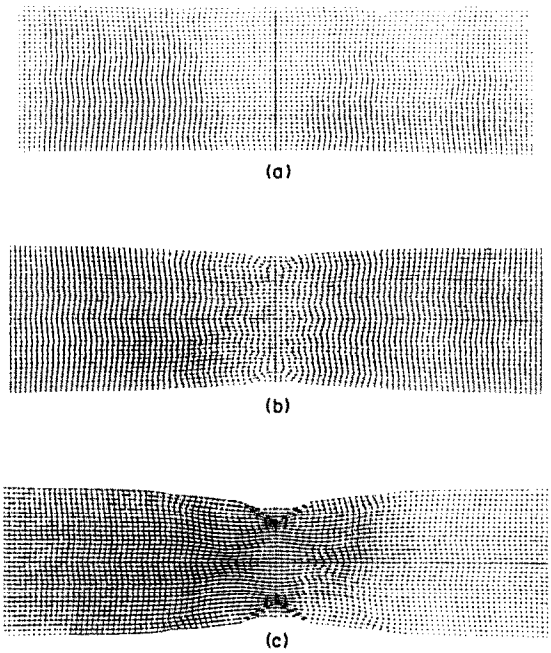

Fig. 17. Deformed finite element meshes corresponding to points marked on the load–displacement curve of Fig. 16. (a) $U/L_0 = 0.10$, (b) $U/L_0 = 0.14$ and (c) $U/L_0 = 0.17$.

The latent hardening here ($q = 1.4$) is high enough so that in a rate independent analysis the parabolic regime is entered and loss of slip uniqueness with prescribed stressing occurs. The rate independent computational procedure of Peirce *et al.* [1] broke down in this regime. Even for the very slightly rate dependent material considered here ($m = 0.001$) no numerical difficulties are encountered although it is necessary to employ small time steps.

The phenomenology of shear band development differs in significant respects from that in the cases discussed previously and Figs 18–20 depict quantitative aspects of this development. As in Fig. 14 a patchy pattern of slip develops in the early stages of deformation. For this nearly rate insensitive crystal the gage breaks up into narrow patches more closely resembling the patchy slip pattern found for rate independent crystals by Peirce *et al.* [1] than the two fairly distinct regions that characterize the more rate dependent crystals discussed above.

In Fig. 18, which corresponds to a state of deformation just beyond the maximum load point, the strain pattern is not highly inhomogeneous as diffuse necking has scarcely begun. However, the slip and rotation patterns are "patchy". At $U/L_0 = 0.14$, Fig. 19, a shear band has developed. This shear band is associated with slip on the primary system and the lattice rotations in the band are consistent with this

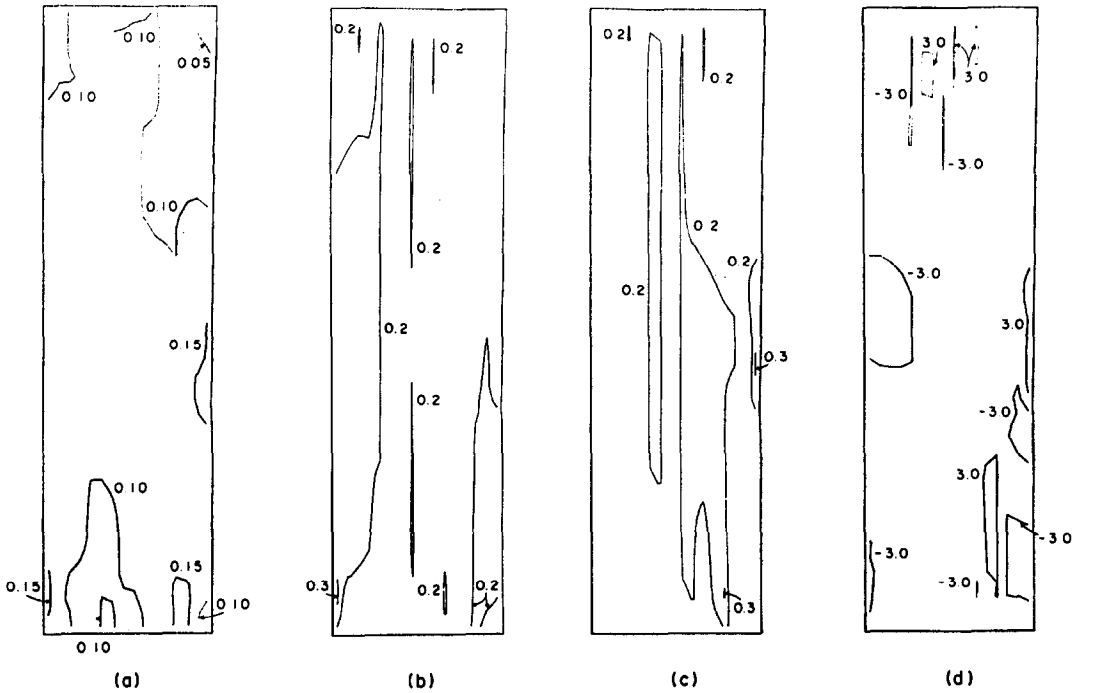

Fig. 18. Contours of strain and lattice rotation in one quadrant of the deformed crystal shown in Fig. 17(a). (a) Contours of constant maximum principal logarithmic strain; (b) contours of constant glide strain on the primary slip system; (c) contours of constant glide strain on the conjugate slip system; and (d) contours of constant rotation (in degrees) of the primary slip direction away from the tensile axis.

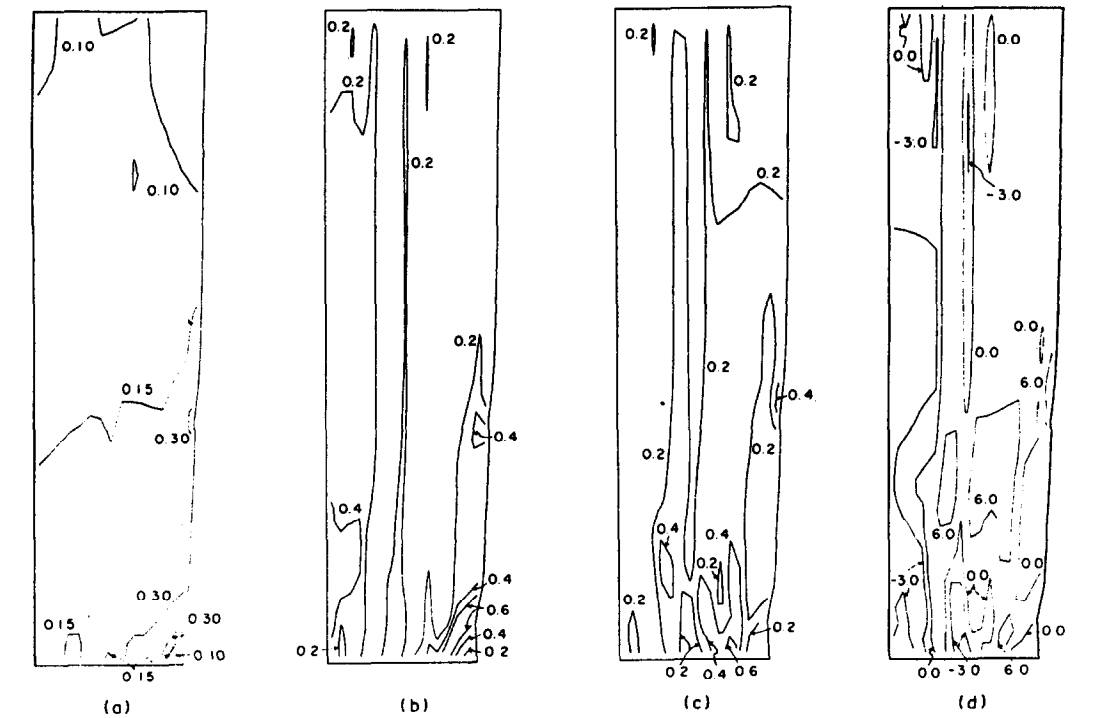

Fig. 19. Contours of strain and lattice rotation in one quadrant of the deformed crystal shown in Fig. 17(b). (a) Contours of constant maximum principal logarithmic strain; (b) contours of constant glide strain on the primary slip system; (c) contours of constant glide strain on the conjugate slip system; and (d) contours of constant rotation (in degrees) of the primary slip direction away from the tensile axis.

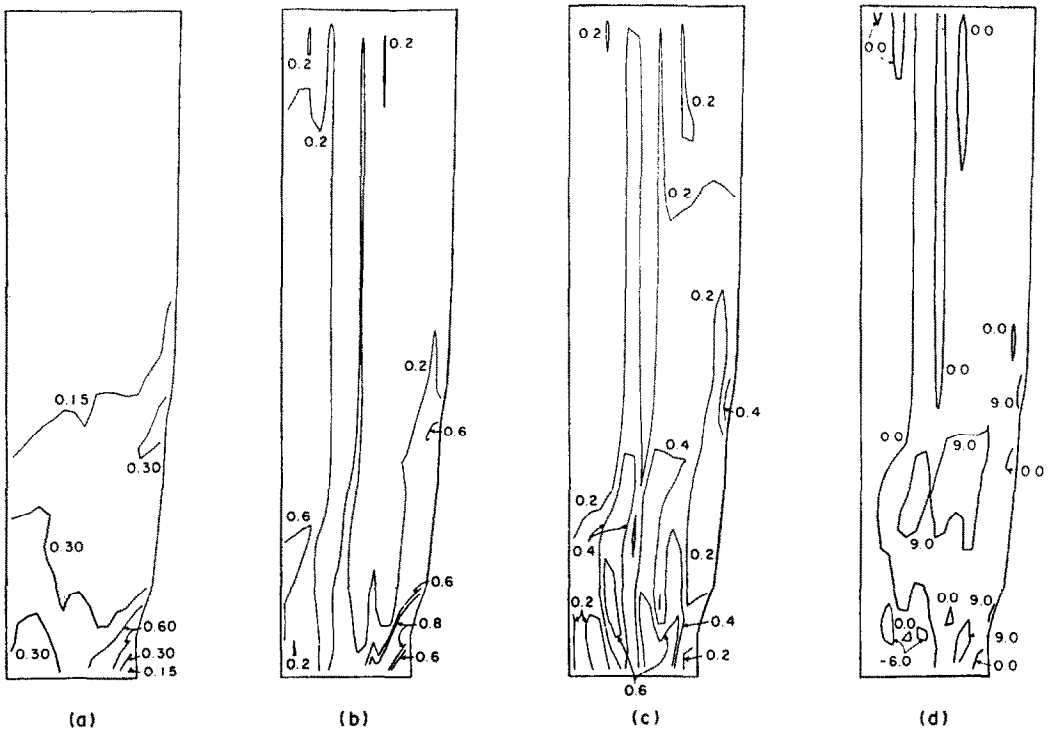

Fig. 20. Contours of strain and lattice rotation in one quadrant of the deformed crystal shown in Fig. 17(c). (a) Contours of constant maximum principal logarithmic strain; (b) contours of constant glide strain on the primary slip system; (c) contours of constant glide strain on the conjugate slip system; and (d) contours of constant rotation (in degrees) of the primary slip direction away from the tensile axis.

slipping mode. The shear band is confined to a region relatively near the free surface, in contrast to the shear band in Figs 9–11, and considerable deformation continues outside the band. Substantial lattice rotations develop [the central 6.0 contours in Fig. 19(d)] which appear unconnected to any shear band. The fully developed shear band is shown in Fig. 20. Note that there is evidence of a second shear band [the 0.3 strain contour in Fig. 20(a) and the 0.6 contour of primary slip in Fig. 20(b)] about one third of the way up along the gage. This is near the location of the shear band in Fig. 8 but propagation of this band across the specimen is inhibited by the "patch" of conjugate slip near the center of the gage. Indeed at the stage of deformation shown in Fig. 20 the lattice misorientations across the gage are so large that it is perhaps inappropriate to regard the specimen as a single crystal. Thus an interesting effect of such strong latent hardening, and patchy slip, is to cause kinematical constraints that prevent shear bands from propagating completely through the gage section. Peirce *et al.* [1] had speculated that a patchy slip pattern with shear bands contained within the patches could develop in crystals with strong latent hardening and this appears to be what has happened. If the shear bands are viewed as a failure mode, then an additional effect of the latent hardening is to increase the crystal's ductility.

3.2.2. Results for b.c.c. crystal simulations. Here, the initial aspect ratio of the crystal is taken to be $L_0/h_0 = 5.1$ and the initial thickness imperfection is of the form (4.5) with $\xi_1 = 0.14 \times 10^{-2}$, $\xi_2 = 0.8 \times 10^{-3}$ and $p = 2$. The shape of the specimen is specified to include the flanges as shown in Fig. 22. Figure 21 displays the computed load vs end-displacement curve along with two others discussed later. The maximum load occurs at a normalized end displacement $U/L_0 = 0.71 \times 10^{-2}$. The development of the deformation pattern after maximum load is illustrated in Fig. 22(c)–(f). The corresponding normalized loads and end displacements are indicated by the cross marks in Fig. 21. The four fold symmetry of the meshes exhibited here is that enforced by the boundary conditions (3.4).

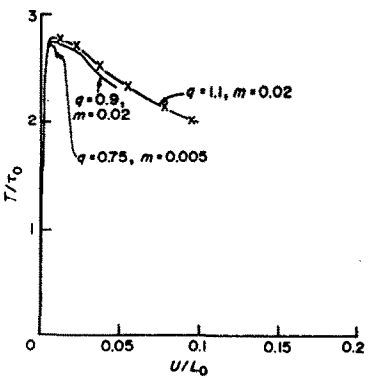

Fig. 21. Normalized load vs end displacement curves for the cases where $\phi = 60°$ and three values of m and q.

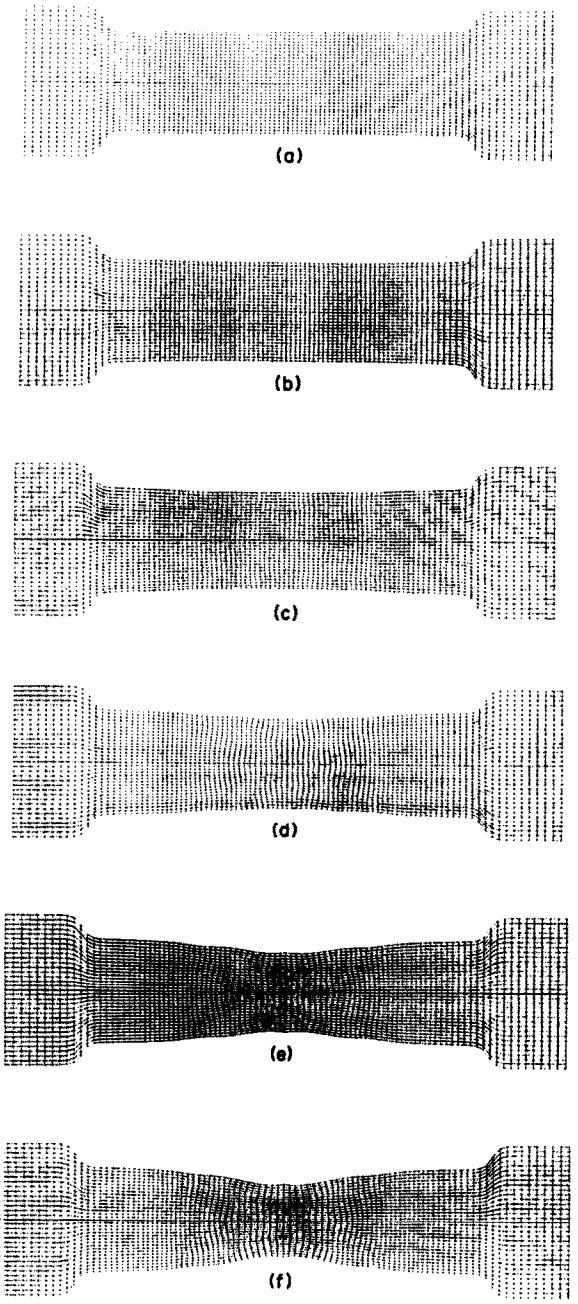

Fig. 22. Deformed finite element meshes for the case where $\phi = 60°$, $q = 1.1$ and $m = 0.02$ corresponding to points marked on the load–displacement curve of Fig. 21. (a) $U/L_0 = 0.011$, (b) $U/L_0 = 0.022$, (c) $U/L_0 = 0.036$, (d) $U/L_0 = 0.052$, (e) $U/L_0 = 0.078$ and (f) $U/L_0 = 0.093$.

In the first two stages of deformation shown in Fig. 22, corresponding to $U/L_0 = 0.011$ and $U/L_0 = 0.022$, the deviation from a homogeneous deformation state is not visible. The development of necking and, subsequently, localized shearing becomes evident at larger end displacements, Fig. 22(c)–(f). Note, however, that a well defined localized shear band does not develop in this case. This contrasts with the behavior exhibited for f.c.c. geometries and, as will be discussed more fully in the following, is a consequence of the difference in kinematics between this geometry and the f.c.c. geometry discussed in Section 2.3.

Various contour plots are shown in Figs 23–28. As before, in each of these figures the first quadrant of the specimen is plotted, with the tensile axis vertical.

In Fig. 23, the small deviations from a homogeneous deformation state are due to the initial thickness imperfection and to the presence of the flange. At this stage of deformation, only slightly beyond the maximum load point, the influence of the flange is at least as great as that of the thickness inhomogeneity.

At $U/L_0 = 0.022$, in Fig. 24, the effect of the diffuse necking mode is evident. Now, the greatest strains and lattice rotations emanate from the surface strain concentrations induced by the initial thickness imperfection. Note the development in Fig. 24(c) of two bands of *conjugate* shear. In Fig. 24(c) one band emanates from the free surface and the other from the symmetry boundary near the center of the crystal. Associated with these bands (Fig. 24(c)) are lattice rotations of the primary system away from the tensile axis. For this geometry ($\phi_0 > 45°$), rotations in this direction give rise initially to geometric softening for the first 15° of rotation and thereafter to geometric *hardening* on the conjugate system. Thus the strain rates eventually must fall, if not vanish, after finite strains.

At the stage of deformation depicted in Fig. 25, which is at $U/L_0 = 0.036$, the contours of constant conjugate shear show a clearly developed band and in Fig. 25(d) the associated lattice rotation. Somewhat above the conjugate shear band on the free surface there is a band of primary slip, with lattice rotations toward the tensile axis, but this band does not propagate into the crystal as far as does the conjugate band. This is anticipated since the primary slip band is propagating away from the neck. Note that there is a significant increase in the lattice rotations between $U/L_0 = 0.022$ (Fig. 24) and $U/L_0 = 0.036$ (Fig. 25) and that, correspondingly, in Fig. 21 there is a substantial load drop between these two stages of deformation. Although the conjugate bands in Figs 25–27 do not have a clear orientation the range of orientations as measured by the angle θ from the tensile axis is $30° \leq \theta \leq 40°$. This is completely expected from the discussion in Section 2.3 and Fig. 6.

The further development of the bands of conjugate shearing is shown in Figs 26 and 27. On the other hand, the band of primary shearing grows relatively little. The load continues to drop significantly and large lattice rotations develop in the conjugate band. It is between the stages corresponding to Figs 26 and 27 that the lattice rotates more than 15° in the conjugate band. Further rotations lead to a reduction in resolved shear stress, a geometric hardening and then to a reduction in strain rate.

As deformation proceeds, the conjugate shearing begins to saturate due to this geometrical hardening. In Fig. 28(c) the conjugate shears are not substantially greater than those in Fig. 27(c) but the band is broadening. The lattice has now rotated so that the

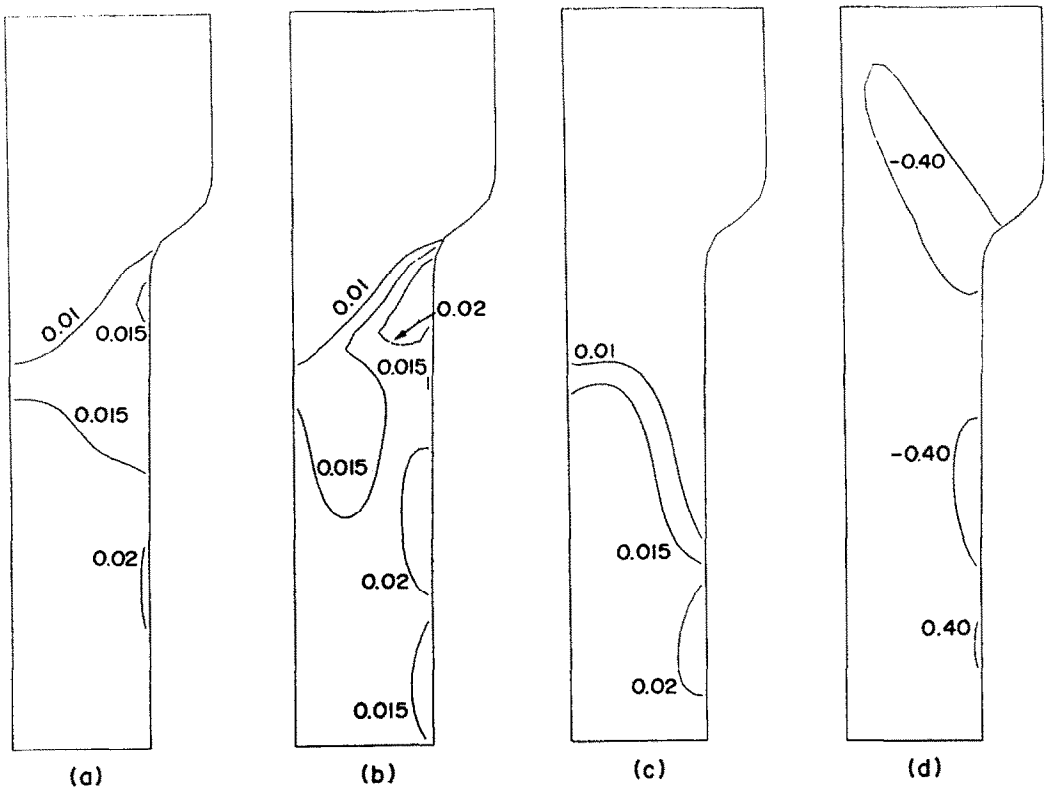

Fig. 23. Contours of strain and lattice rotation in one quadrant of the deformed crystal shown in Fig. 22(a). (a) Contours of constant maximum principal logarithmic strain; (b) contours of constant glide strain on the primary slip system; (c) contours of constant glide strain on the conjugate slip system; and (d) contours of constant rotation (in degrees) of the primary slip direction away from the tensile axis.

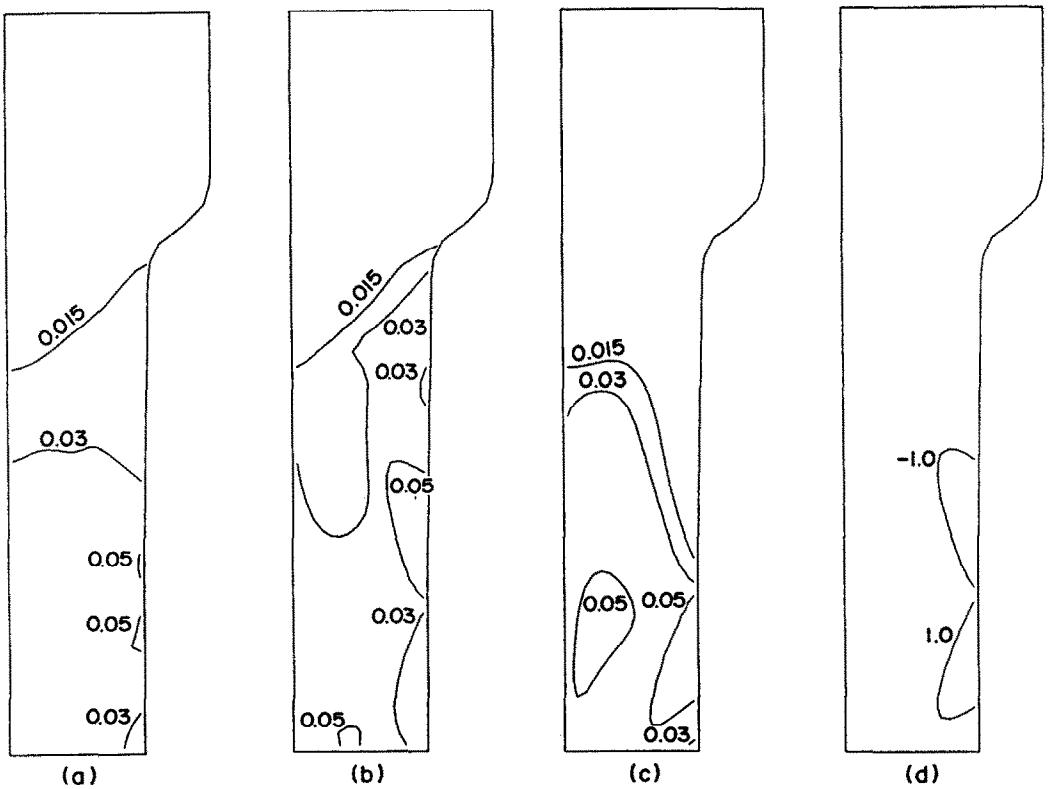

Fig. 24. Contours of strain and lattice rotation in one quadrant of the deformed crystal shown in Fig. 22(b). (a) Contours of constant maximum principal logarithmic strain; (b) contours of constant glide strain on the primary slip system; (c) contours of constant glide strain on the conjugate slip system; and (d) contours of constant rotation (in degrees) of the primary slip direction away from the tensile axis.

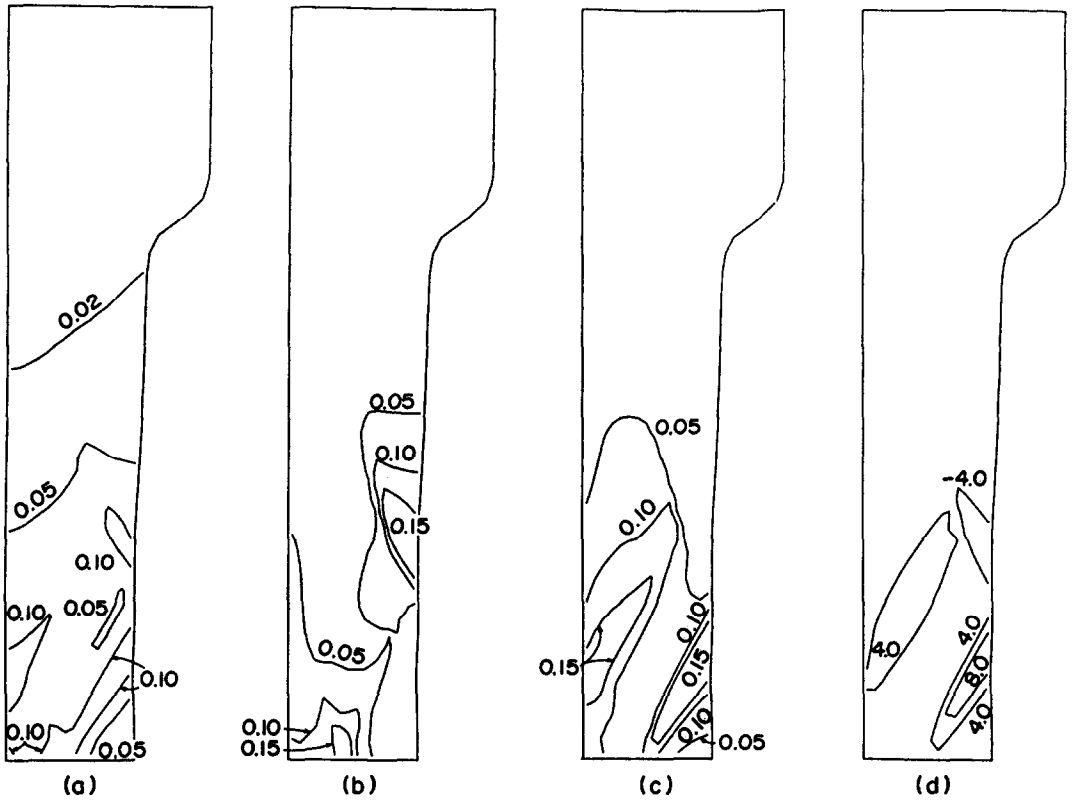

Fig. 25. Contours of strain and lattice rotation in one quadrant of the deformed crystal shown in Fig. 22(c). (a) Contours of constant maximum principal logarithmic strain; (b) contours of constant glide strain on the primary slip system; (c) contours of constant glide strain on the conjugate slip system; and (d) contours of constant rotation (in degrees) of the primary slip direction away from the tensile axis.

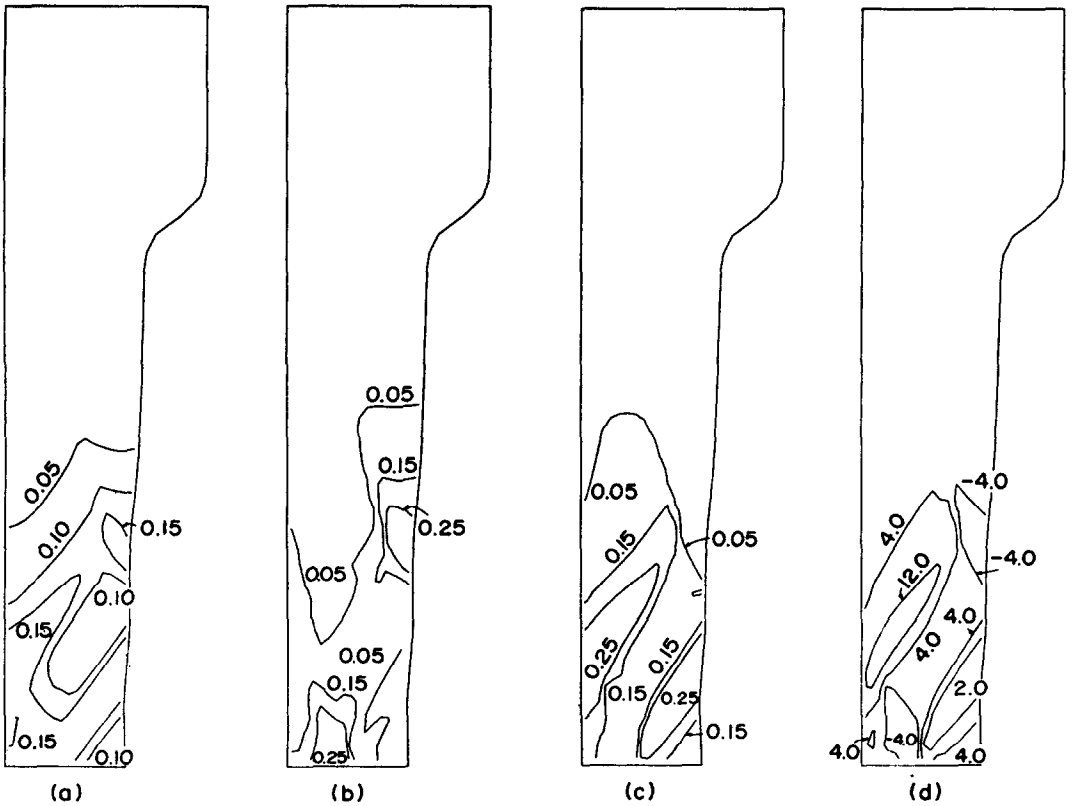

Fig. 26. Contours of strain and lattice rotation in one quadrant of the deformed crystal shown in Fig. 22(d). (a) Contours of constant maximum principal logarithmic strain; (b) contours of constant glide strain on the primary slip system; (c) contours of constant glide strain on the conjugate slip system; and (d) contours of constant rotation (in degrees) of the primary slip direction away from the tensile axis.

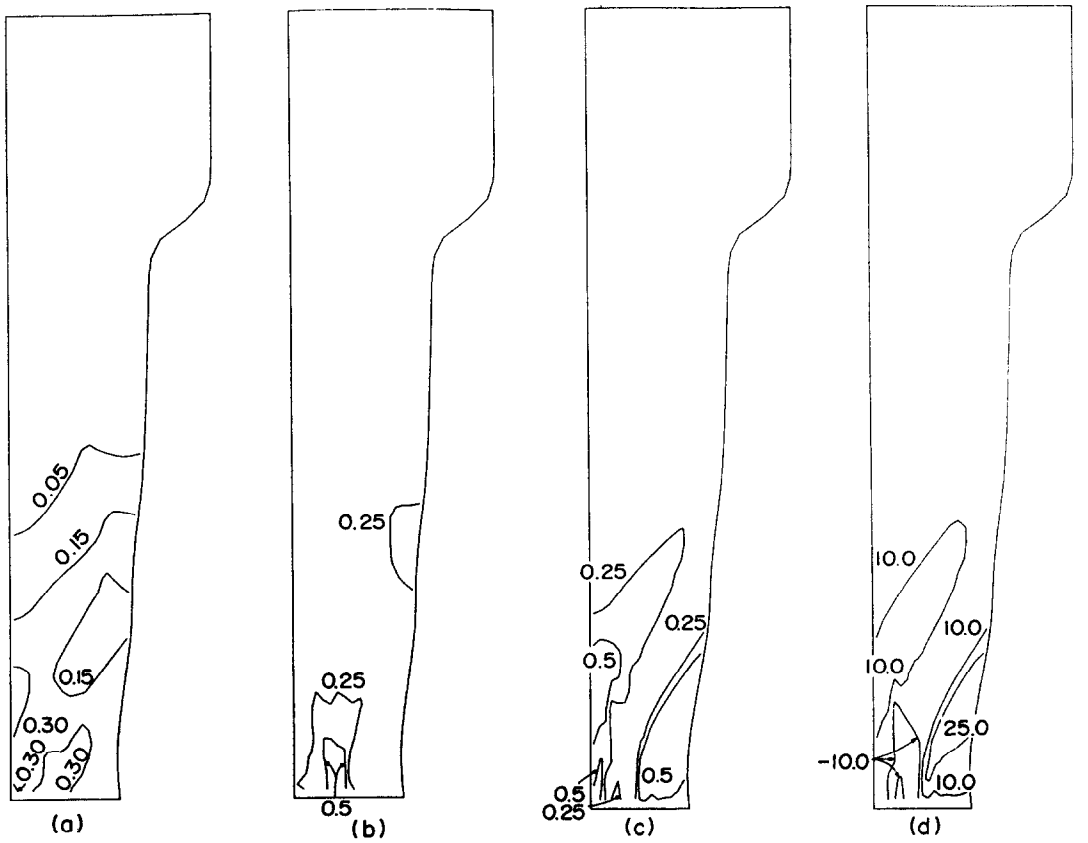

Fig. 27. Contours of strain and lattice rotation in one quadrant of the deformed crystal shown in Fig. 22(e). (a) Contours of constant maximum principal logarithmic strain; (b) contours of constant glide strain on the primary slip system; (c) contours of constant glide strain on the conjugate slip system; and (d) contours of constant rotation (in degrees) of the primary slip direction away from the tensile axis.

resolved shear stress in the band emanating from the free surface has nearly vanished (when the lattice rotates 30°, which it has in the interior of the band, the resolved shear stress on the conjugate system does indeed vanish).

The phenomenology of deformation just described is quite general for this crystal model when $\phi = 60°$. What changes noticeably, however, is the load vs displacement behavior. Some typical results are shown in Fig. 22 for two other combinations of m and q. A principal effect of reduced strain rate sensitivity (smaller m) is to accentuate the load drop. The three cases shown in Fig. 22 used the same slip plane hardening law given earlier for $\phi = 60°$ and so the change in strain hardening behavior is reflected only through changes in q.

4. DISCUSSION

Our rate dependent finite element calculations have again shown the vital role of lattice kinematics in the development of nonuniform and localized modes of deformation. In those cases where $\phi = 30°$ we find that shear bands form which are closely aligned with the most dominant slip system in the bands. The kinematics of this mode involve lattice rotations in the bands which increase the resolved shear stress on that system, i.e. the rotations cause a "geometrical softening", and thus promote continued locally intense straining. When $\phi = 60°$ in the model, which represents a very different sort of geometry, shear bands have difficulty forming and instead localized modes which we have called "bands of secondary slip" emerge. These are bands of intensified slip which are aligned more closely with the less active of the two available slip systems. The lattice rotations that occur in these bands are such that at first the more active system (i.e. the conjugate system) is geometrically softened and then hardened. Because of this the strain rates eventually fall off. Since all the material strain hardening laws used in the calculations describe strictly hardening materials, the results also demonstrate that strain softening behavior is not required to observe shear bands or other localized modes of deformation.

Rate sensitivity has a marked effect on the quantitative aspects of the phenomenology. For example, the curves marked I and II in Fig. 7 show that even a modest rate sensitivity corresponding to $m = 0.005$ significantly affects the load–strain behavior after maximum load and the initiation of nonuniform deformation. When the rate sensitivity becomes sufficiently high, e.g. $m = 0.02$ in this calculation, shear

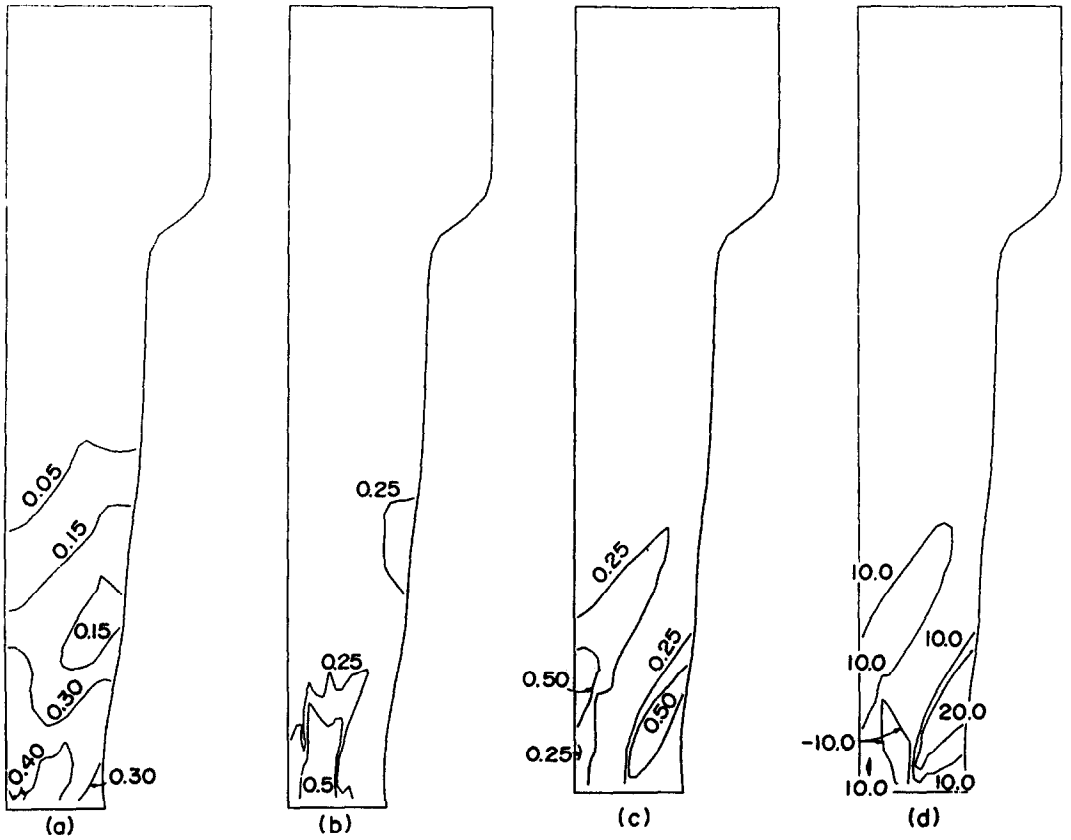

Fig. 28. Contours of strain and lattice rotation in one quadrant of the deformed crystal shown in Fig. 22(f). (a) Contours of constant maximum principal logarithmic strain; (b) contours of constant glide strain on the primary slip system; (c) contours of constant glide strain on the conjugate slip system; and (d) contours of constant rotation (in degrees) of the primary slip direction away from the tensile axis.

band formation is greatly retarded, and may be effectively precluded, and therefore the crystal's ductility is greatly increased.

Another interesting and very important part of the phenomenology uncovered in the present development is the effect of "patchy slip associated with high latent hardening on the patterns of deformation at large strain. Here it is important to recall that high latent hardening (and particular geometries) tends to cause the governing equations to become parabolic in which case the numerical procedures break down in the rate independent theory. In addition, when μ becomes negative—also caused by high latent hardening—there is a loss in slip mode uniqueness for prescribed stress rates. In the rate dependent formulation presented here we encountered no such limitations or numerical difficulties; our studies covered the range $0.75 \leq q \leq 1.8$. Now if the calculation corresponding to Figs 7, (curve II), 8 and 9–11 is compared to that corresponding to Figs 16, 17 and 18–20 a set of important effects are revealed.

The rather high latent hardening ratio of $q = 1.4$ used in the calculation of Figs 16–20 causes a pronounced pattern of patchy slip to develop; this is clearly developed after an elongation of 10% in Fig. 18. The patches persist and after an additional elongation of 4% the patches have developed rather large lattice misorientations as shown in Fig. 19(d). The slip plane strain hardening law, i.e. $h(\gamma)$, used in this calculation is identical to that used to produce Figs 7–11 and the strain rate sensitivity is a factor of 5 lower. Thus we expect shear bands to form in Fig. 17 as in Fig. 8. Figures 17(c) and 20 indeed show that bands do form—there are two primary shear bands evident in Figs 17(c) and 20(b). However, if the contours of glide strain in Fig. 20(c) which mark the bands are compared to the contours of lattice rotation shown in Fig. 20(d), it becomes clear why the bands do not, or cannot, easily propagate through the gage. The rather abrupt changes in lattice rotation create a sort of crystallographic constraint. An associated effect is that the load drop after maximum load is less abrupt as can be seen by comparing Figs 7, (curve II) and 16 and it is entirely likely that the net achievable strain would be much larger as a result. There are indeed numerous examples where shear bands or intense slip bands are contained within the gage section of crystals of materials with high latent hardening. An example can be found in the α-brass crystals tested by Piercy *et al.* [26] (see Peirce *et al.* [1] for some discussion). Related examples are found in the numerous cases of what appear to be shear bands confined within either individual grains or clusters of grains in polycrystals [27, 28]. Whether the bands do not propagate into or through neighboring grains

because of an orientation or texture mismatch is not clear but the present observations suggest this may be one reason. Of course after larger strains accumulate these confined bands may be made to coalesce to form bands extending through the single crystal or polycrystalline specimen. A failure mechanism of this type was described by Hahn and Rosenfield [27] in aluminum alloys; the coalesced bands were called "super bands".

The development of a rate dependent constitutive framework for analyzing crystalline plasticity at large strain as presented here certainly makes possible the study of other phenomena and other types of boundary value problems. These studies are vital for developing a clear and accurate understanding of crystal plasticity. In particular, it is possible, at least in principle, to include more complex crystal models and even those based on the actual 3-dimensional geometries of f.c.c. or b.c.c. crystals. Any such calculations, however, should be based on either experimental observations if these are available or should be coupled to experiments so that a more precise description of rate dependent crystalline plasticity can be obtained.

One particularly interesting extended calculation would be for the last case considered in Section 3, i.e. for $\phi = 60°$. In this case our model of Fig. 2 bears a rough similarity to the niobium crystals tested by Reid *et al.* [4]. Their crystals oriented for tension along a $\langle 111 \rangle$ direction exhibited a predominantly double mode of slip. The slip systems in this case were each oriented such that single slip on either would tend to induce "geometrical softening" on the active slip system which corresponds to the case where $\phi > 45°$. When the crystals were tested at low temperatures, e.g. 77 K, the deformation was highly localized in thin shear bands and was described by them as catastrophic. They also noted that the slip mode in the bands was apparently more complex than simple double slip but the actual kinematics were difficult to describe precisely; they speculated that the actual slip mode could have been a complex mode of composite slip on several other systems (and other slip planes). Our results suggest that the rather strong temperature dependence of the strength and strain rate sensitivity of niobium would certainly favor shear bands at low temperatures. However what is perhaps equally important, but not yet studied, is the effect of slip on *other systems* on the localization process. The large rotations induced in the "bands of secondary slip" shown in Figs 25–28 would undoubtedly influence the rate of slipping on other systems had these been included in the model.

Based on our calculations we can suggest the following mechanism for the catastrophic shearing observed by Reid *et al.* [4]. First, a secondary slip band forms as in Figs 25–28. Then, the load drops abruptly, with a more abrupt load drop occurring at low temperatures due to the decreased rate sensitivity. For a finite stiffness loading device, the load drop may be sharp enough for an instability to be encountered (in our calculations we prescribe the tensile displacement, which is the infinitely stiff loading device limit), with the observed failure mode involving slip on systems geometrically softened by the lattice rotations accompanying the secondary slip band. This sort of mechanism is intriguing in that it suggests that the secondary slip band mode induces failure by acting as a transition mode to the final failure mode observed. This proposed mechanism is speculative and a full 3-dimensional calculation based on the actual b.c.c. geometry would be needed in order to properly describe the kinematics.

The present theory also points the way to formulating much more accurate large strain models for polycrystals and clearly this should be pursued. In particular, it would seem that the problem of texture development in polycrystals can now be reformulated so that a unique prediction of texture and its dependence on strain hardening-latent hardening behavior, and strain rate sensitivity, is possible. The question of how texture affects polycrystalline constitutive behavior could be addressed in these models as well—with the hopeful end result being a more accurate theory of large strain elastic–plastic behavior of crystalline materials in general.

Acknowledgements—R.J.A. gratefully acknowledges support from the Metallurgy Section of the U.S. National Science Foundation under grant DMR26190. D.P. is grateful for the support provided by the Materials Research Laboratory at Brown University, funded by the U.S. National Science Foundation. A.N. gratefully acknowledges the support of the U.S. National Science Foundation (Solid Mechanics Program) under grant MEA-8101948. The computations reported on here were carried out on the Brown University, Division of Engineering, VAX-11/780 computer. The acquisition of this computer was made possible by grants from the U.S. National Science Foundation (Grant ENG78-19378), the General Electric Foundation and the Digital Equipment Corporation.

REFERENCES

1. D. Peirce, R. J. Asaro and A. Needleman, *Acta metall.* **30**, 1087 (1982).
2. G. I. Taylor, *J. Inst. Metals.* **62**, 307 (1938).
3. J. Pan and J. R. Rice, *Int. J. Solids Struct.* To be published.
4. C. N. Reid, A. Gilbert and G. T. Hahn, *Acta metall.* **14**, 975 (1966).
5. J. Sawkill and R. W. K. Honeycombe, *Acta metall.* **2**, 854 (1954).
6. G. I. Taylor and C. F. Elam, *Proc. R. Soc. Lond.* **A102**, 643 (1923).
7. G. I. Taylor and C. F. Elam, *Proc. R. Soc. Lond.* **A108**, 28 (1925).
8. J. R. Rice, *J. Mech. Phys. Solids* **19**, 433 (1971).
9. R. Hill and J. R. Rice, *J. Mech. Phys. Solids* **20**, 401 (1972).
10. J. W. Hutchinson, *Proc. R. Soc. Lond.* **A348**, 101 (1976).
11. J. W. Hutchinson, *Proc. R. Soc. Lond.* **A319**, 247 (1970).
12. R. J. Asaro, *Acta metall.* **27**, 445 (1979).
13. R. Hill, *J. Mech. Phys. Solids* **6**, 236 (1958).
14. R. J. Asaro, in *Adv. appl. Mech.* To be published.
15. U. F. Kocks, *Metall. Trans.* **1**, 1121 (1970).
16. Y. W. Chang and R. J. Asaro, *Acta metall.* **29**, 241 (1981).
17. M. Biot, *Mechanics of Incremental Deformations.* Wiley, New York (1965).

18. R. Hill and J. W. Hutchinson, *J. Mech. Phys. Solids* **23**, 239 (1975).
19. V. Tvergaard, A. Needleman and K. K. Lo, *J. Mech. Phys. Solids* **29**, 115 (1981).
20. I. C. Cormeau, *Int. J. Num. Meth. Engng* **9**, 109 (1975).
21. C. F. Shih, H. G. deLorenzi and A. K. Miller, *SMIRT-4 Proc.*, Paper L212 San Francisco (1977).
22. K. J. Willam, *Comput. Struct.* **8**, 511 (1978).
23. R. M. Zirin and E. Krempl, ASME Paper 80-C2/PVP-33 (1980).
24. M. M. Little, E. Krempl and C. F. Shih, On the time and loading rate dependence of crack tip fields at room temperature—A viscoplastic analysis of tensile small scale yielding. To be published.
25. D. Peirce, C. F. Shih and A. Needleman, *Comput. Struct.* In press.
26. G. R. Piercy, R. W. Cahn and A. H. Cottrell, *Acta metall.* **3**, 331 (1955).
27. G. T. Hahn and A. R. Rosenfield, *Metall. Trans.* **6A**, 653 (1975).
28. L. Anand and W. A. Spitzig, *J. Mech. Phys. Solids* **28**, 113 (1980).
29. J. W. Hutchinson, *J. Mech. Phys. Solids* **21**, 163 (1973).